

Electrical readout of spins in the absence of spin blockade

Felix-Ekkehard von Horstig,^{1,2,*} Lorenzo Peri,^{1,3} Virginia N. Ciriano-Tejel,¹ Sylvain Barraud,⁴ Jason A. W. Robinson,² Monica Benito,⁵ Frederico Martins,⁶ and M. Fernando Gonzalez-Zalba^{1,†}

¹*Quantum Motion, 9 Sterling Way, London, N7 9HJ, United Kingdom*

²*Department of Materials Sciences and Metallurgy, University of Cambridge, Charles Babbage Rd, Cambridge CB3 0FS, United Kingdom*

³*Cavendish Laboratory, University of Cambridge,*

JJ Thomson Ave, Cambridge CB3 0HE, United Kingdom

⁴*CEA, LETI, Minatec Campus, F-38054 Grenoble, France*

⁵*Institute of Physics, University of Augsburg, 86159 Augsburg, Germany*

⁶*Hitachi Cambridge Laboratory, J.J. Thomson Avenue, CB3 0HE, United Kingdom*

(Dated: October 9, 2025)

In semiconductor nanostructures, spin blockade (SB) is the most scalable mechanism for electrical spin readout requiring only two bound spins for its implementation. In conjunction with charge sensing techniques, SB has led to high-fidelity readout of spins in semiconductor-based quantum processors. However, various mechanisms may lift SB, such as strong spin-orbit coupling (SOC) or low-lying excited states, hence posing challenges to perform spin readout at scale and with high fidelity in such systems. Here, we present a method, based on the dependence of the two-spin system polarizability on energy detuning, to perform spin state readout even when SB lifting mechanisms are dominant. It leverages SB lifting as a resource to detect selectively different spin measurement outcomes. We demonstrate the method using a hybrid system formed by a quantum dot (QD) and a Boron acceptor in a silicon p-type transistor and show spin selective readout of different spin states under SB lifting conditions due to (i) SOC and (ii) low-lying orbital states in the QD. We further use the method to determine the detuning-dependent spin relaxation time of 0.1-8 μ s. Our method should help perform projective spin measurements with high spin-to-charge conversion fidelity in systems subject to strong SOC, will facilitate state leakage detection and enable complete readout of two-spin states.

I. INTRODUCTION

Direct measurement of individual spins is an extremely challenging task given their small magnetic dipole moment. However, in semiconductor nanostructures, the charge dipole associated with electron tunnelling can be sizeable. Such divide in electronic properties is reflected in the vastly different state-of-the-art sensitivities for the spin (~ 10 spins/ $\sqrt{\text{Hz}}$ [1–3]) and charge degrees of freedom ($\sim 10^{-6}$ electrons/ $\sqrt{\text{Hz}}$ [4–6]) which has pushed researchers to develop spin-to-charge conversion (SCC) techniques in conjunction with charge sensing for electrical spin readout. Energy filtering, for example, uses the difference in tunnel rates to a charge reservoir of Zeeman-split spins states confined to a quantum dot (QD) (or impurity) [7] whereas spin blockade (SB) uses quantum selection rules to inhibit tunnelling between two-particle states with different spin numbers [8], see Figure 1. In particular, SB is a more scalable mechanism for SCC requiring only two bound spins for its implementation and has proven instrumental in achieving high fidelity readout of spin qubits [9–12] even at low magnetic fields [13] and high temperatures [14, 15].

Charge sensing, in conjunction with SCC mechanisms as described above, relies on bi-state measurements arising from the charge sensor detecting either charge tunneling or the lack thereof. This means that only a specific subset of spin measurement outcomes may trigger the charge detector, while the absence of such trigger may be attributed to the complementary subset [16]. However, this approach has drawbacks, including potential state leakage or spin mapping errors [17]. Furthermore, various mechanisms may lift SB, such as strong spin-orbit coupling (SOC) – which allows two-particle states with different spin numbers to couple (Figure 1b) [18, 19] – and low valley-orbit level splitting – allowing symmetric spin states to exist in different orbital or valley states of the same confining potential (Figure 1c) [20, 21]. The former mechanism is particularly relevant to spins III-V materials [22–25] and novel spin qubit systems such as holes in germanium [26–29], and silicon QDs [30–32] that have come at the forefront of semiconductor based quantum computing due their technical ease for spin manipulation via electric fields [33–37] and their potential for large scale integration [38, 39]. A key element in the operation of spin qubits in double QDs is rapid spin projection(separation) pulses through a singlet-triplet anticrossing which are utilized to read(initialize)

* felix@quantummotion.tech

† fernando@quantummotion.tech

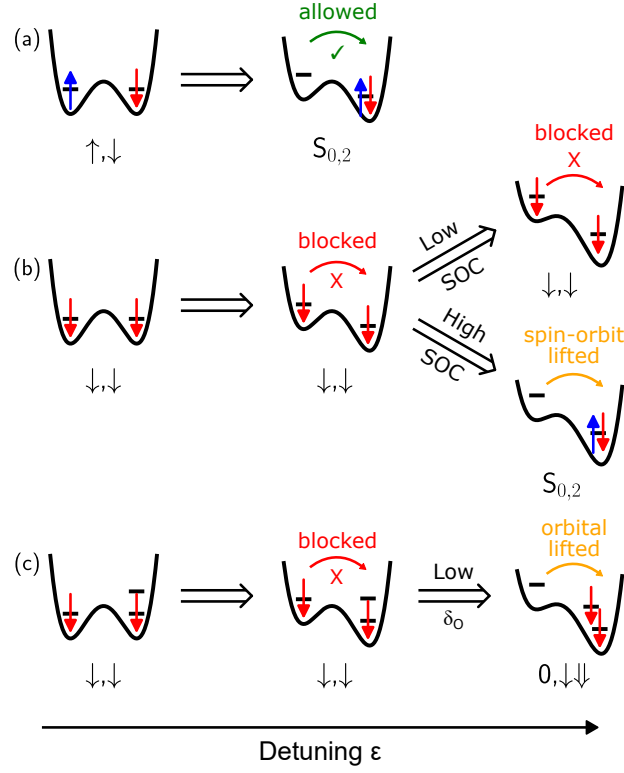


FIG. 1. Spin readout using spin-blockade: (a) Anti-symmetric spins allow for the movement of spins, while (b,c) symmetric spins are blocked, allowing for the two-particle spin states to be distinguished. At increased detuning, SB can be lifted in the presence of either large spin-orbit interaction (b) or the presence of low-lying excited orbital states of energy δ_o (c).

the system [40]. However, the anisotropic nature of SOC on these systems results in magnetic field orientations in which SOC is strongly enhanced which may compromise satisfying the diabatic condition of the pulses and hence the ultimate achievable readout and initialization fidelity in scaled up systems (see Supplementary Note 1).

To overcome these challenges, we present a methodology, based on dispersive readout techniques [41] and spin-to-charge-polarizability conversion [42] that utilizes the very same coupling between states that leads to SB lifting, as a resource for selective readout of the states of a two-spin system. More concretely, our methodology makes use of the energy-detuning-dependent charge polarizability of the two-spin system to positively detect the spin measurement outcome without the need to perform a rapid diabatic pulse through a singlet-triplet anticrossing, minimising SCC mapping errors. The difference in polarizability manifests itself as a state-dependent quantum capacitance that can be detected through the dispersive interaction with a microwave superconducting resonator [43]. We demonstrate this readout methodology using a hybrid system subject to strong SOC formed by a hole QD and a Boron acceptor in a silicon nanowire transistor and measure its spin relaxation time as a function of energy detuning. Finally, we expand the readout methodology to systems with low-lying orbital states, where SB may be lifted by allowed tunnelling to the higher energy orbital. We implement the demonstration in a different charge configuration of our hybrid system, and show that the spin states can be mapped onto signals arising from the orbital ground and excited state charge transitions, allowing for the spin states to be measured selectively.

II. RESULTS

A. Spin blockade lifting via spin-orbit coupling

We use a p-type single-gate silicon transistor with light Boron channel doping, a system subject to strong SOC (Figure 2a) [44]. By applying a voltage on the top-gate (V_g) and back-gate (V_{bg}), we accumulate holes in QDs formed in the nanowire, as well as in individual Boron atoms (Figure 2b). We connect the gate of the transistor to a superconducting microwave (mw) resonator (panel a), to detect quantum capacitance changes arising from mw-driven cyclic charge tunnelling between the QD/Boron and the source and drain charge reservoirs (S,D) as well as between

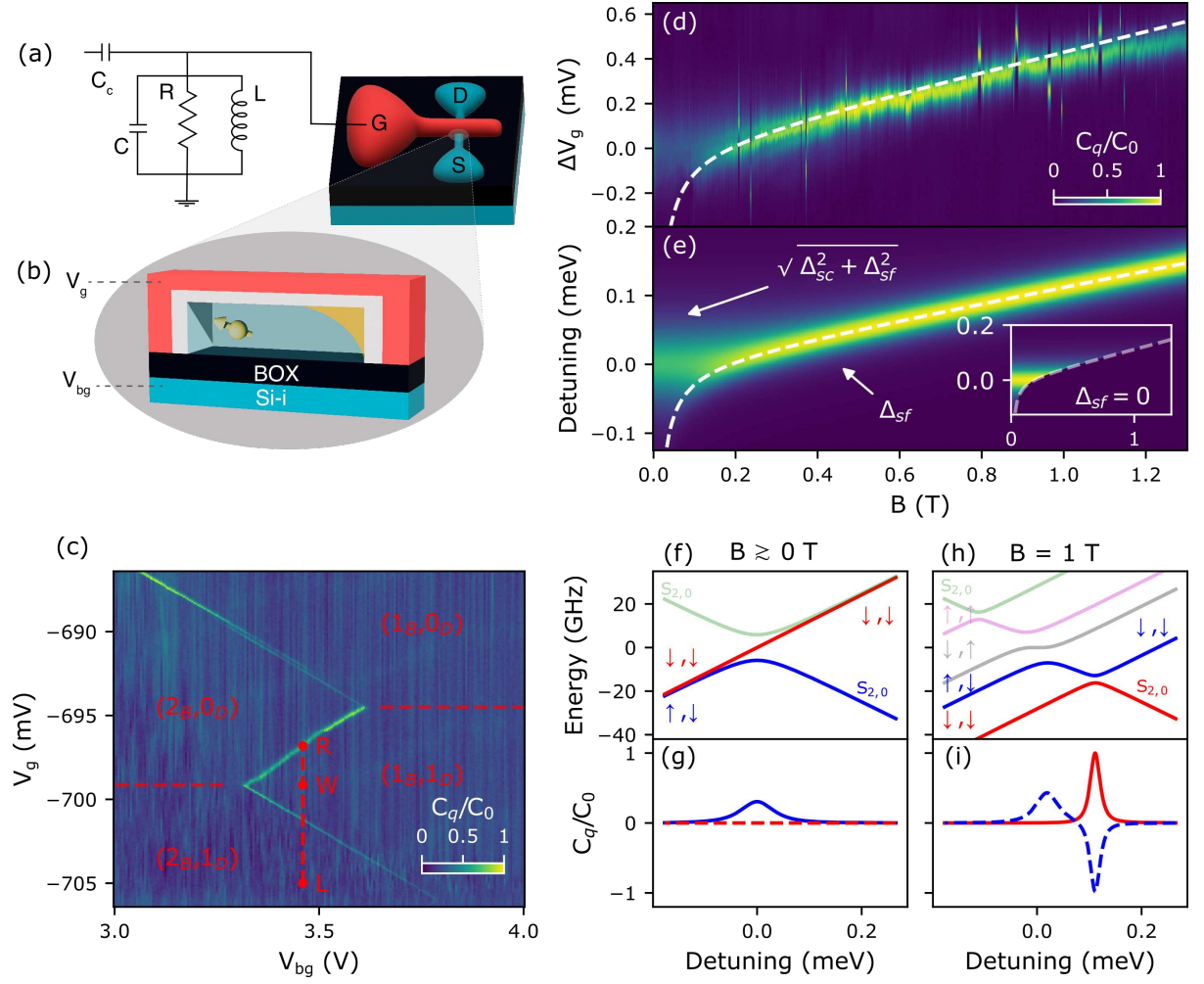


FIG. 2. Device description and readout concept: (a) Schematic of silicon nanowire transistor (top-view), labelled with Source (S), Drain (D) and top-gate (G) contacts, embedded in an LCR resonator for charge readout. (b) Schematic side-view of Si-nanowire with gate stack including gate metal (red), gate oxide (grey), channel (transparent blue), buried oxide (BOX in black) and intrinsic silicon substrate (Si-i, also blue). The corner QD and Boron atom where holes are confined are marked in yellow. (c) Charge stability diagram showing the capacitive signal measured in the V_g - V_{bg} space near the boron-dot transition (positive slope). A boron-reservoir transition is also visible (negative slope). The charge occupation are annotated in the plot. The approximate location of the dot-reservoir transition is indicated in red dashed lines. Location of Load, Wait and Read voltages for readout measurements are marked in red. (d) Magneto-spectroscopy measurement near the point labelled R in the stability diagram. The dotted line shows the location of the $T_{1,1}/S_{2,0}$ anticrossing. (e) Simulated magneto-spectroscopy of the same transition. The insert shows a simulation of the same transition with $\Delta_{sf} = 0$, showing the emergence of SB. (f,h) Energy level diagram at two magnetic fields. (g,i) Capacitive signal of the lowest two states (\uparrow_B, \downarrow_D) and ($\downarrow_B, \downarrow_D$) at two magnetic fields. In each case the excited state is plotted in dashed lines.

QDs and Boron atoms. We refer to the latter as interdot charge transitions (ICTs).

We tune the device to an ICT between a Boron atom and a QD (ICT A) with nominal charge occupation of $(N_B, N_D) = (1,1)/(2,0)$ (Figure 2c) and a gate lever arm asymmetry $\Delta\alpha = 0.26 \pm 0.03$, a parameter used to convert gate voltage to energy detuning between the QD and Boron atom, see Supplemantar Note 2 for the full charge stability map. Throughout this work, we provide state occupations in the form (B,D), where the first will refer to the state of the Boron atom and the second to that of the QD. To characterise the spin eigenstates of the system, we perform magneto-spectroscopy [45] by measuring the resonator response, which at low temperature ($k_B T \ll \Delta_{sc}, \Delta_{sf}$ as defined below) corresponds to the quantum capacitance, C_q , of the ground state of the system, against gate voltage across the ICT and magnetic field strength applied in the plane of the sample (Figure 2d).

The data reveals an enhancement of the resonator response which shifts up in V_g as the magnetic field is increased above $B \approx 0.2$ T. This is the signature of an effective two-spin system subject to strong SOC where, above 0.2 T, the system is free to tunnel between the polarised triplet state ($\downarrow_B, \downarrow_D$) and the joint singlet ($S_{2,0}$) [46]. The enhancement

in the signal originates from the reduced tunnel coupling of the $\downarrow_B, \downarrow_D$ (ground state above $B \approx 0.2$ T) compared with the \uparrow_B, \downarrow_D (ground state below $B \approx 0.2$ T) with the $S_{2,0}$ state. This is SOC-mediated spin blockade lifting which we describe in detail below.

We consider the two-particle SOC Hamiltonian in Supplementary Note 3 that takes into account the g -factor of the Boron(QD) $g_{B(D)}$ (where in our case $g_B < g_D$) and the spin-conserving and spin-flip tunnel coupling, Δ_{sc} and Δ_{sf} . In Figure 2e, we plot the simulated magneto-spectroscopy, as well as the eigenenergies and capacitive signals (Figure 2 f,h and g,i) arising from the lowest two states at $B = 0(1)$ T. For $B < 0.2$ T, the capacitive signal arises from charge tunneling between the ground (\uparrow_B, \downarrow_D) and $S_{2,0}$ states, mediated by the finite Δ_{sc} , see blue trace in panel g. For $B > 0.2$ T, however, the signal arises from the tunneling between the Zeeman split $T_{1,1}^- = (\downarrow_B, \downarrow_D)$ and the $S_{2,0}$ state, in this case mediated by Δ_{sf} , see the red trace in panel i. The good match between the experiment and simulations confirms the presence of the lifting mechanism since, for systems with low SOC, like few-electron QDs in silicon, such spin-flip tunneling processes are forbidden resulting in the signal vanishing asymmetrically at high fields (see the simulation in the insert of Figure 2e) [47].

Magneto-spectroscopy allows us to quantify the parameters in the Hamiltonian. First, we obtain the average g -factor of the hole spin in the QD and Boron, $\bar{g} \sim 2$, which is given by the slope of the transition in the $T_{1,1}^-/S_{2,0}$ regime ($\bar{g} = e\alpha\Delta V_g/\mu_B B$), where e is the electron charge and μ_B the Bohr magneton [48]. Further, from the linewidth of the signal at zero and high field ($T_{1,1}^-/S_{2,0}$ regime), we extract the total charge and spin-flip coupling rates, $\sqrt{2}\Delta_c = \sqrt{\Delta_{sc}^2 + \Delta_{sf}^2} \sim 10.4$ GHz and $\Delta_{sf} \sim 3.4$ GHz, respectively. Additionally, by measuring the shift in V_g of the Boron-reservoir transition with magnetic field (not shown), we find the g -factor of the Boron $g_B \sim 1.6$ making the g -factor of the QD, $g_D \sim 2.4$.

B. Spin readout under spin-orbit lifted SB

Spin blockade is based on the exclusion principle in which two fermionic particles cannot possess all the same quantum numbers. It is utilized in DQDs to project the combined spin state of two separated spin carrying particles into that of a single QD whose ground state is the joint singlet, $S_{2,0}$. Particularly, the polarized Triplets $T_{1,1}^\pm$ are blocked from transitioning into $S_{2,0}$ a feature that is used for spin parity readout, or for Singlet-Triplet readout if the unpolarized triplet state T^0 is also blocked [49].

In the presence of SOC, however, Δ_{sf} enables tunnelling of the $T_{1,1}^\pm$ states into the $S_{2,0}$, eliminating the spin selectivity of SB readout via projective measurements unless a fast diabatic pulse across the Δ_{sf} anticrossing can be performed. Such a requirement may be challenging in practice given that the Δ_{sc} anticrossing also needs to be crossed adiabatically, ultimately limiting the fidelity of the SCC mechanism (see Supplementary Note 1).

In this work, we use Δ_{sf} to our advantage. The finite spin flip coupling term between the $T_{1,1}^-$ and $S_{2,0}$ spin branches generates a distinct anticrossing at positive energy detuning ε . Most critically, for the purpose of our demonstration, we note that the capacitive signals arising from the anticrossings of the aligned ($\downarrow_B, \downarrow_D$) and anti-aligned (\uparrow_B, \downarrow_D) spin outcomes occur at different detuning (see the red and blue traces in Figure 2i respectively), a concept that we exploit in the following for spin readout.

We note two additional features of this readout scheme that may be used to distinguish the other spin states, $T_{1,1}^+ = (\uparrow_B, \uparrow_D)$ and $(\downarrow_B, \uparrow_D)$, from the $T_{1,1}^-$ and $(\uparrow_B, \downarrow_D)$ states: First, the $T_{1,1}^+$ and $(\downarrow_B, \uparrow_D)$ additionally anticross with the $S_{0,2}$ state at a third and fourth readout point at negative detuning (see Figure 2h), allowing for these populations to be distinctly measured (Supplementary Note 4). Second, beyond a positive and negative C_q , also a neutral response can be measured. This allows for the spin states producing a C_q to be additionally distinguished from those that do not (see Supplementary Note 5). For example, assuming the spin states were adiabatically transferred from the (1,1), at the anticrossing between the $T_{1,1}^-$ and $S_{2,0}$ states, a positive (or negative) C_q would correspond to a $T_{1,1}^-$ (or $(\uparrow_B, \downarrow_D)$) measurement outcome respectively, while a neutral response indicates either a $T_{1,1}^+$ or $(\downarrow_B, \uparrow_D)$ state. Together, these two techniques may be used to measure the full spin state of the two-spin system (Supplementary Note 4.1).

To measure the spin of the Boron, we first randomly initialise the system in either $(\uparrow_B, \downarrow_D)$ or $T_{1,1}^-$. We do so by starting in the $(2_B, 1_D)$ charge state (point L in Figure 2c) to then pulse into the $(1_B, 1_D)$ region (point W), which randomly unloads a spin from the Boron atom, as illustrated in Figure 3a. We then pulse to either of the readout points (R_A, R_P where the subscripts stand for anti-parallel and parallel) and measure the dispersive signal in the time domain, see Figure 3d-f. For these preliminary experiments, we set the wait time at W to $t_W = 0$ s. Additionally, we perform a control measurement in which we wait in the (1,1) region to deterministically initialize the system in the $T_{1,1}^-$ by relaxation (see pulse sequences in Figure 3c and Methods).

We observe two signals at different detuning (panel d), the separation of which depends on the magnetic field intensity as anticipated (see Supplementary Note 6). When we take a cut at zero detuning (panel e), we observe the

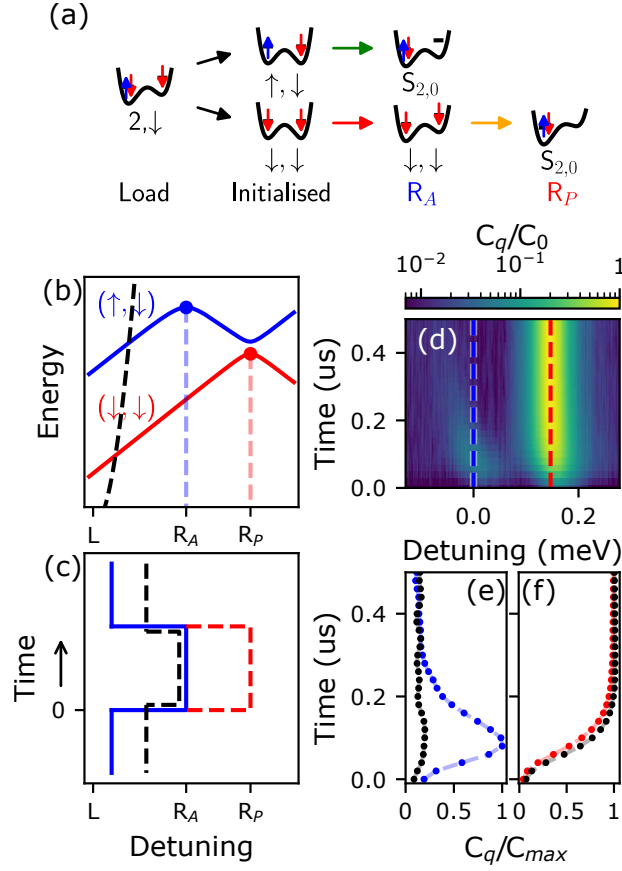


FIG. 3. Readout protocol with spin-orbit coupling: (a) Schematic of pulsing scheme. The state is initialised by randomly unloading a spin from the Boron atom starting from a $(2, \downarrow)$ configuration resulting in either a $(\downarrow_B, \downarrow_D)$, or a $(\uparrow_B, \downarrow_D)$. The measurement is performed either at R_A [triggered by the $(\uparrow_B, \downarrow_D)$ state] or at R_P [triggered by the $(\downarrow_B, \downarrow_D)$ state]. (b) Energy level diagram showing the load (L) and read points for the two states (R_A , R_P). The black dashed line denotes the Boron-reservoir transition between the $(2,1)$ and the $(1,1)$ charge states. (c) Schematic of pulse sequence for spin readout. States are initialised at L, and then pulsed to either R_A or R_P (blue or red lines). The black dashed lines indicates the control pulse where the state is initialised in the $(1,1)$ region. The time at which data acquisition is started is indicated. (d) Capacitive signal as a function of measurement time and detuning showing two signal arising from the $(\downarrow_B, \downarrow_D)$ and $(\uparrow_B, \downarrow_D)$ states. R_A and R_P are indicated with dashed lines. Measurements carried out at $B = 1$ T. (e,f) Line-cuts of d at detuning of R_A and R_P showing the capacitive signal (normalised to the peak value of each trace) against time. Dashed lines are given as a guide to the eye. The black lines are the signals recorded from the control measurement.

signal from the $(\uparrow_B, \downarrow_D)$ - $S_{2,0}$ anticrossing, i.e. a $(\uparrow_B, \downarrow_D)$ measurement outcome. The signal initially rises, due to the finite ring up of the resonator, before decaying with a time constant $T_1 \sim 100$ ns given by the relaxation time to the $T_{1,1}^-$ state (blue trace). We highlight a slower decay in the signal from the $(\uparrow_B, \downarrow_D)$ measurement at more negative detuning, which we attribute to a detuning-dependent T_1 which we investigate further in the following Section. We note that the short T_1 at the readout point prevented us from performing single-shot readout measurements (see Supplementary Note 7 for further discussion).

At finite positive detuning (R_P), on the other hand, we observe signals arising from the $T_{1,1}^-$ - $S_{2,0}$ anticrossing, i.e. a $T_{1,1}^-$ measurement outcome (Figure 3f). In this case, the signal (red trace) is delayed with respect to the resonator ring up (black trace). The slower dynamics is caused by the fraction of $(\uparrow_B, \downarrow_D)$ shots that carry a negative quantum capacitance at R_P , hence reducing the signal at timescales comparable to the relaxation time of 95 ns in this case.

Our result shows that, in spin systems with lifted SB due to SOC, the spin state can be read using the different detuning points at which the dispersive signal of the $(\uparrow_B, \downarrow_D)$ and $T_{1,1}^-$ measurement outcomes manifest. This measurement is done without the need to perform a perfectly diabatic pulse through the $T_{1,1}^-$ - $S_{2,0}$ anticrossing.

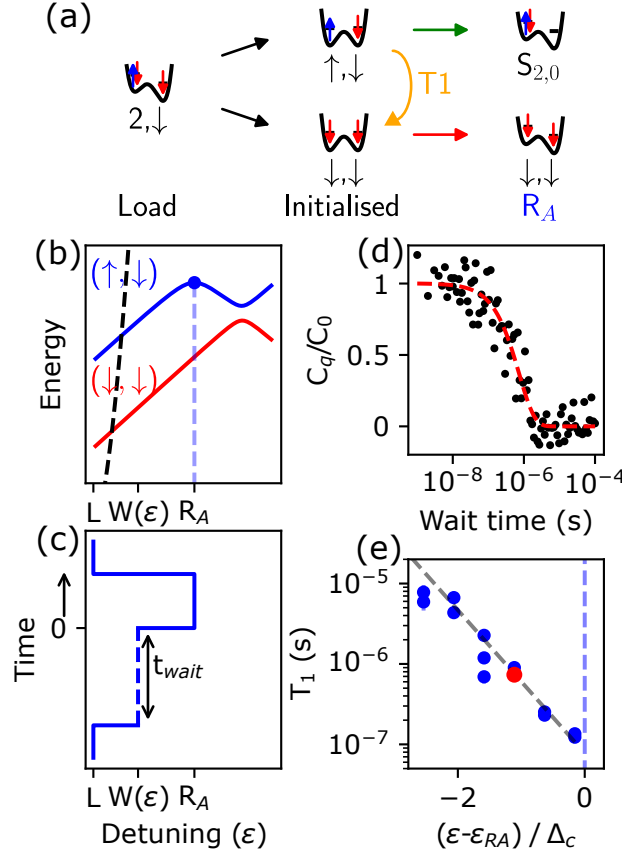


FIG. 4. T_1 characterisation: Measurements carried out at $B = 700$ mT. (a-c) Schematic of the measurement protocol: The state is initialised as described in Figure 3. This is followed by a Wait ($W(\epsilon)$) period of variable time and pulse depth in which $(\uparrow_B, \downarrow_D)$ may relax into $T_{1,1}^-$. Finally the state is read out at the spin anti-parallel readout point (R_A). The location of $W(\epsilon)$ is varied to characterise T_1 as a function of ϵ . The time at which data acquisition is started is indicated. (d) Example capacitive signal [a proxy for the $(\uparrow_B, \downarrow_D)$ population] against t_w at $\epsilon = -92 \mu\text{eV} = -1.12 \Delta_c$ (red dot panel e). The data is taken from the maximum signal of line traces similar to that in Figure 3d. The data is fitted using an exponential decay to extract T_1 (730 ± 80 ns in this case). (e) T_1 against detuning of the wait location $W(\epsilon)$ showing an exponential dependence (black dashed line) with detuning. The location of R_A is marked in blue. The data in panel d is marked with a red dot.

C. Spin relaxation time

To demonstrate the benefit of this spin readout mechanism, we now study the spin qubit decay constant T_1 as a function of detuning. We again initialise randomly in the $(\uparrow_B, \downarrow_D)$ or $T_{1,1}^-$ state but wait in the (1,1) region (point $W(\epsilon)$) for a variable time before pulsing to the readout point R_A (Figure 4a-c). For long t_w , the initialised state will have a higher chance to decay to the ground state resulting in a reduction in the average excited state signal (Figure 4d). We extract T_1 by fitting the data to an exponential decay of the form $P_S(t_w) \propto \exp(-t_w/T_1)$ (red dashed line). We repeat this measurement for different detuning points and find that T_1 increases exponentially away from the readout point (Figure 4e) up to $8 \mu\text{s}$, increasing its utility as a spin qubit.

We hypothesize the short T_1 at the readout point is caused by the coupling of the spin and charge degrees of freedom, i.e. at the anticrossing, the spin-carrying charges have the largest dipole and therefore are most impacted by charge noise. We note that a charge relaxation time, $T_1 = 100$ ns has been measured in a similar sample [50].

To further support the hypothesis, we discard spin-orbit coupling as the dominant source of relaxation at the readout point due to lack of dependence of T_1 with magnetic field [51] (see Supplementary Note 6), where we show several time-dependent readout signal similar to that reported in Figure 3 but recorded at different magnetic fields.

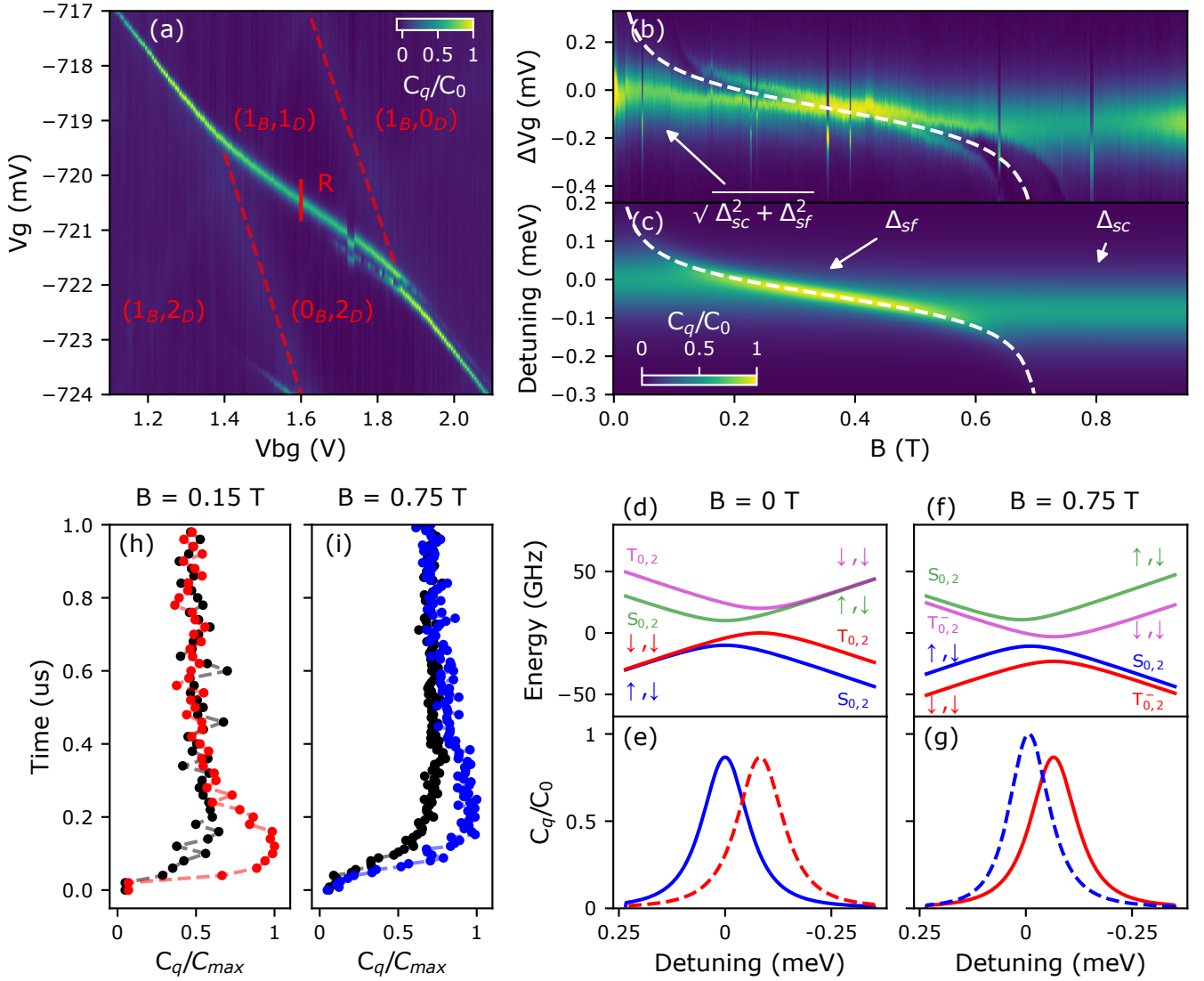


FIG. 5. Readout utilising orbital states: (a) Stability diagram of ICT B showing the nominal charge occupation. The readout location is highlighted. (b,c) Magneto-spectroscopy and simulation at the point marked R in a. (d,f) Energy level diagrams showing the energy levels of the transition at two magnetic fields. (e,g) Capacitive signals from the $(\uparrow_B, \downarrow_D)/S_{0,2}$ (blue) and $T_{1,1}^-/T_{0,2}^-$ (red) anticrossings marking the two readout locations. In each case the excited state is marked in dashed lines. (h,i) Capacitive signal measured, used to distinguish $(\uparrow_B, \downarrow_D)$ and $T_{1,1}^-/T_{0,2}^-$ states (low magnetic field) or the $(\uparrow_B, \downarrow_D)/S_{0,2}$ transition (high magnetic field) as readout points. The response is normalised to the maximum of each linetrace.

D. Spin readout under orbitally lifted SB

In projective SB measurements, the presence of low-lying excited orbital or valley states (of energy δ_o) lifts SB by allowing spin triplets ($T_{0,2}$) to exist in the $(0,2)$ charge configuration. Hence, when the energy detuning exceeds δ_o , both triplet and singlet are allowed to transition into the $(0,2)$, eliminating spin selectivity of the charge movement (Figure 1c). Although techniques are available to increase the energy of the δ_o , for example by moving to a $(1,3)$ charge occupation to fill the lowest valley in electron systems [52] or by reducing the size of the QD to increase orbital energies, the excited states still impact the readout of using projective SB. This mechanism limits the magnetic fields at which SB can be performed in transport measurements to $B < \delta_o/(\bar{g}\mu_B)$ [20], while in charge-sensing experiments it limits the size of the voltage window in which SB can be detected [53].

In this Section, we demonstrate that the readout mechanism described in the context of SOC, naturally extends to anticrossings arising from orbital states. In particular, we show that instead of being a constraint, the presence of orbital states can be used as a resource by resulting in two distinct readout locations which can be used to measure the

spin state of the hybrid DQD. Such approach allows to selectively and positively detect different spin measurement outcomes. While this method does not increase the size of the readout window as compared to standard charge-sensed SB, it provides an alternate methodology to read the spin state dispersively.

For the demonstration, we tune the device to a different ICT comprising a different Boron atom and QD (ICT B) with nominal charge occupation $(N_B, N_D) = (1, 1)/(0, 2)$ and differential lever arm $\Delta\alpha = 0.54 \pm 0.02$ (Figure 5a). Notably, in the (0,2) configuration the two holes reside within the QD, in contrast to ICT A where they resided in the Boron. The presence of low-energy orbital excited states in the QD allow for an orbital lifting of SB. We perform magneto-spectroscopy and again find an enhancement of the signal at magnetic fields above 300 mT characteristic of a two-spin-system with SOC. However, in this case, we additionally find that above 600 mT the signal remains at a fixed V_g point and its intensity is reduced, the signature that a transition from $T_{1,1}^-$ to the $T_{0,2}^-$ state involving an orbital excitation in the QD is now allowed [21].

From magnetospectroscopy (Figure 5b), we extract $\Delta_c \sim 20$ GHz, $\Delta_{sf} \sim 4$ GHz, $\delta_o \sim 20$ GHz, where δ_o is the QD excited state energy. From the slope of the transition in the $T_{1,1}^-/S_{0,2}$ and the $T_{0,2}^-$ regimes, we extract the average g -factor, $\bar{g} = 2.1 \pm 0.1$, and g -factor difference $\delta g = g_B - g_D = 0.3 \pm 0.1$, respectively. We extend the Hamiltonian to include the $T_{0,2}^-$ state (Supplementary Note 3) and simulate the magnetospectroscopy in Figure 5c. In the data, we note the additional edges in the signal parallel to the $T_{1,1}^-/S_{0,2}$ anticrossing (white dashed line), see Figure 5b. These arise due to resonant interactions between the spin system and photons in the mw resonator (2.1 GHz). Although less clear, these can also be observed in Figure 2d.

We plot the energy-level diagrams and capacitance from the ground and first excited states at $B = 0$ T and $B = 0.75$ T in Figure 5d-g. For ease of readability, we only include the $T_{1,1}^-$ and $(\uparrow_B, \downarrow_D)$ states in the (1,1) charge region and the $T_{0,2}^-$ in the (0,2) region. We further set $\Delta_{sf} = 0$, since it is less relevant at fields explored in this section, i.e. outside the intermediate field regime where the T^-/S anticrossing occurs. At magnetic fields below and above the T^-/S regime, two distinct readout points emerge corresponding to the $(\uparrow_B, \downarrow_D)/S_{0,2}$ anticrossing (ground state at low magnetic field), and the $T_{1,1}^-/T_{0,2}^-$ anticrossing (ground state at high magnetic fields), separated in detuning by $\delta_o + [(g_B - g_D^*)/2]\mu_B B$, where g_D^* is the g -factor of the excited state of the doubly occupied QD.

We now demonstrate readout in each of these regimes. First, at low field ($B = 0.15$ T), we use the $T_{1,1}^-/T_{0,2}^-$ anticrossing as the readout point. We start deep in the (1,1) region, where the ground state is $T_{1,1}^-$, to then perform a diabatic passage through the $T_{1,1}^-/S_{0,2}$ anticrossing to prepare the system in the excited $T_{1,1}^-$ state near zero detuning. Finally, we ramp to the $T_{1,1}^-/T_{0,2}^-$ anticrossing and gather the time-domain response (red points in Figure 5h). We observe an initial resonator ring-up followed by a decay with $T_1 \sim 140 \pm 50$ ns (see Methods). In this case, the signal does not fully decay to zero as it was the case for the SOC experiments. This is a particularity of our concrete experiments since the signal from the ground state can also be detected at the readout point since $\delta_o \lesssim \Delta_c$ (note the overlap in the C_q peaks in Figure 5e and g). We discuss this limitation further in Supplementary Note 9. We compare the signal to a control measurement where we initialise in the ground state deep in the (0,2) region by waiting for relaxation to the $S_{0,2}$ state. We then ramp to the readout point (black points). In this case, the system remains in the ground state and the signal rises with the ring up of the resonator.

For the high field case ($B=0.75$ T), where we use the $(\uparrow_B, \downarrow_D)/S_{0,2}$ anticrossing for readout, we perform a similar sequence but starting deep in the (0,2) region where the ground states is $S_{0,2}$. Via diabatic pulsing through the $T^-/S_{0,2}$ anticrossing (outside the detuning range of panel f), we prepare the system in the excited $S_{0,2}$ near zero detuning to then ramp to the readout point. We observe a similar resonator ring-up followed by a decay with now a $T_1 \sim 270 \pm 50$ ns. We plot the data and the control in Figure 5i.

By measuring the decay constant as a function of detuning near the readout points, we find that T_1 ranges between 100-200 ns (200-400 ns) in the low (high) magnetic field case, with larger values reported further from the readout point. We hypothesize that the difference in T_1 for the two cases is related to the state decay happening primarily between the $T_{0,2}$ and $S_{0,2}$ at low fields - a spin decay within the QD - while at high magnetic fields the decay occurs between the $(\uparrow_B, \downarrow_D)$ and $(\downarrow_B, \downarrow_D)$ states - a decay within the Boron atom.

Overall, our results show that, in spin systems with lifted SB due to orbital states, the spin state can be read selectively and positively by making use of the different detuning points at which the dispersive signal of the $(\uparrow_B, \downarrow_D)$ and $T_{1,1}^-$ measurement outcomes manifest. While SOC is present in our system, resulting in a finite Δ_{sf} and g -factor difference, neither are required for readout using orbital states, allowing the readout mechanism to be extended to systems lacking strong SOC such as electrons in silicon. In such systems ($\Delta_{sf} = 0$, $g_D = g_B$), the two readout points correspond to a Singlet or Triplet (T^\pm , T^0) outcome. We discuss this further in Supplementary Note 4.2.

III. DISCUSSION

We have presented a novel spin readout methodology based on the detuning-dependent polarizability of the two-spin system in a semiconductor DQD to perform spin readout even when SB lifting mechanisms are present. We demonstrate this readout mechanism in two situations: Readout in the presence of SOC leading to spin flip tunnel coupling between the T^- and $S_{2,0}$ states, and spin-blockade lifting due to the presence of excited orbital states.

We note that, going beyond the applications presented in the experimental section, our methodology enables three-valued readout, where up to three different spin sub-states can be discerned with a single measurement at a given measurement point (see Supplementary Note 5). This is a consequence of the charge polarization nature of the method where a positive, negative and neutral response of the system can be detected. The tri-state and selective nature of our measurements may therefore enable complete readout of the state of two-spin systems more efficiently than what is possible through charge sensing [54], reducing the number of necessary repetitive measurements [55] (see Supplementary Note 4.1).

Our work and methodology opens new opportunities to (i) study the fundamentals of SB, its angular dependence in SOC systems and its impact on the ultimate readout fidelity. We highlight the limit of typical charge-sensed SB protocols to perform SCC due to incomplete diabatic passage of the $\uparrow, \uparrow/S_{2,0}$ anticrossing (see Supplementary Note 1). Since the method presented in this work does not require any diabatic passages it may be a way to enable high SCC fidelity. (ii) The ability to use the selective and tri-state nature of the readout may be used to enhance the spin readout fidelity, detect state leakage and complete readout of two-spin systems without the need of perturbative tunnel barrier pulses [54]. In particular, by successively measuring at the various readout points of the spin-orbit coupled system, the full spin state, as well as state leakage out of the computational subspace may be detected (see Supplementary Note 4.1). (iii) Our work encourages the exploration of hybrid QD-acceptor systems and its interaction with a microwave resonator as a system for quantum information processing. This work shows interesting promise that in these systems the spin-relaxation time may be improved, increasing their utility as potential qubits. The acceptor (which can be seen as a hole analogue to a phosphorus donor) produces tight confinement, increasing the energy of orbital states.

METHODS

Fabrication details. The transistors used in this study consists of a single gate silicon-on-insulator (SOI) nanowire transistor with a channel width of 120 nm, a length of 60 nm and height of 8 nm on top of a 145-nm-thick buried oxide. The silicon layer has a Boron doping density of $5 \cdot 10^{17} \text{ cm}^{-3}$. The silicon layer was patterned to create the channel using optical lithography, followed by a resist trimming process. The transistor gate stack consists of 1.9 nm HfSiON – leading to a total equivalent oxide thickness of 1.3 nm – capped by 5 nm TiN and 50 nm polycrystalline silicon. After gate etching, a Si_3N_4 layer (10 nm) was deposited and etched to form a first spacer on the sidewalls of the gate, then 18-nm-thick Si raised source and drain contacts were selectively grown before source/drain extension implantation and activation annealing. A second spacer was formed, followed by source/drain implantations, an activation spike anneal and salicidation (NiPtSi). The nanowire transistor and superconducting resonator were connected via Al/Si 1% bond wires.

Measurement set-up. Measurements were performed at the base temperature of a dilution refrigerator ($T \sim 10 \text{ mK}$). Low frequency signals (V_g, V_{bg}) were applied through Constantan twisted pairs and RC filtered at the MXC plate. Radio-frequency signals were applied through filtered and attenuated coaxial lines to a coupling capacitor at the input of the LC resonator. Fast pulsing signals were applied through attenuated coaxial CuNi lines to an on-PCB (printed circuit-board) bias-T connected to the source of the transistor. The resonator (characteristic frequency 2.1 GHz) consists of a NbTiN superconducting spiral inductor ($L \sim 30 \text{ nH}$), coupling capacitor ($C_c \sim 40 \text{ fF}$) and low-pass filter fabricated by *Star Cryoelectronics*. For exact details of the superconducting chiplet see ref. [43]. The PCB was made from 0.8-mm-thick RO4003C with an immersion silver finish. The reflected rf signal was amplified at 4 K and room temperature, followed by quadrature demodulation (Polyphase Microwave AD0540B), from which the amplitude and phase of the reflected signal were obtained (homodyne detection).

Readout pulse sequence. The data in Figure 3d consists of 100,000 shots at each detuning point, resulting in an average resonator response of the initialised states. After the readout measurement cycle in Figure 3c, we wait for 100 microseconds in the (1,1) region to ensure the spin in the QD has decayed to the \downarrow ground state. This ensures only the (\uparrow_B, \downarrow_D) and ($\downarrow_B, \downarrow_D$) states can be initialised. For the time domain data (Figure 3d-f), the time constant of the resonator ring-up ($\tau \sim 80 \text{ ns}$) is in good agreement with the bandwidth of our resonator ($\kappa/2\pi \sim 3\text{-}4 \text{ MHz}$ with the exact value depending on magnetic field, and $\tau = 2/\kappa$). For readout at R_A , we estimate the state decay constant T_1 from the exponential decay of the signal after the initial rise. For readout at R_P , the initialised signal rises more slowly ($\tau \sim 95 \text{ ns}$) as compared to the control ($\tau \sim 80 \text{ ns}$).

Fit of time traces to extract T_1 at the readout point. To extract the state decay constants from the time-traces in Figure 3 e and Figure 5h and i, we fit the data with a model combining the ring-up of the resonator (determined by $\tau \sim 80$ ns) with capacitive signal contributions arising from the ground (C_{gnd}) and excited state (C_{exc}) where the excited state exponentially decays into the ground determined by a time constant T_1 :

$$C_{\text{total}} = \left(1 - e^{-\frac{t}{\tau}}\right) \left[C_{\text{exc}} e^{-\frac{t}{T_1}} + C_{\text{gnd}} \left(1 - e^{-\frac{t}{T_1}}\right)\right], \quad (1)$$

where t is the measurement time. We use a least square fit to extract T_1 and estimate the uncertainty from the covariance of the fit.

ACKNOWLEDGEMENT

This research was supported by the UK's Engineering and Physical Sciences Research Council (EPSRC) via the Cambridge NanoDTC (EP/L015978/1). F.E.v.H. acknowledges funding from the Gates Cambridge fellowship (Grant No. OPP1144). J.W.A.R. acknowledges funding from the EPSRC Core-to-Core International Network Grant "Oxide Superspin" (No. EP/ P026311/1). M.F.G.Z. acknowledges a UKRI Future Leaders Fellowship [MR/V023284/1]. L.P. acknowledges support from The Winton Programme for the Physics of Sustainability. MB acknowledges funding from the Emmy Noether Programme of the German Research Foundation (DFG) under grant no. BE 7683/1-1.

AUTHOR CONTRIBUTIONS

F.E.v.H. acquired and analysed the data under the supervision of M.F.G.Z. and J.W.A.R. and F.M.. F.E.v.H., L.P. and M.F.G.Z. conceived and designed the experiment and contributed to the writing of the manuscript. L.P. developed the spin modelling under supervision by M.F.G.Z and M.B.. S.B. fabricated the CMOS device.

DATA AVAILABILITY

The source data that support the plots within this article and other findings of this study are provided with this study.

COMPETING INTERESTS

The authors declare no competing interests.

-
- [1] A. Bienfait, J. J. Pla, Y. Kubo, M. Stern, X. Zhou, C. C. Lo, C. D. Weis, T. Schenkel, M. L. W. Thewalt, D. Vion, D. Esteve, B. Julsgaard, K. Mølmer, J. J. L. Morton, and P. Bertet, Reaching the quantum limit of sensitivity in electron spin resonance, *Nat. Nanotechnol.* **11**, 253 (2016).
 - [2] V. Ranjan, S. Probst, B. Albanese, T. Schenkel, D. Vion, D. Esteve, J. J. L. Morton, and P. Bertet, Electron spin resonance spectroscopy with femtoliter detection volume, *Appl. Phys. Lett.* **116**, 184002 (2020).
 - [3] R. P. Budoyo, K. Kakuyanagi, H. Toida, Y. Matsuzaki, and S. Saito, Electron spin resonance with up to 20 spin sensitivity measured using a superconducting flux qubit, *Appl. Phys. Lett.* **116**, 194001 (2020).
 - [4] R. J. Schoelkopf, P. Wahlgren, A. A. Kozhevnikov, P. Delsing, and D. E. Prober, The radio-frequency single-electron transistor (RF-SET): A fast and ultrasensitive electrometer, *Science* **280**, 1238 (1998).
 - [5] A. Aassime, G. Johansson, G. Wendin, R. J. Schoelkopf, and P. Delsing, Radio-frequency single-electron transistor as readout device for qubits: Charge sensitivity and backaction, *Phys. Rev. Lett.* **86**, 3376 (2001).
 - [6] S. Schaal, I. Ahmed, J. A. Haigh, L. Hutin, B. Bertrand, S. Barraud, M. Vinet, C.-M. Lee, N. Stelmashenko, J. W. A. Robinson, J. Y. Qiu, S. Hacoen-Gourgy, I. Siddiqi, M. F. Gonzalez-Zalba, and J. J. L. Morton, Fast gate-based readout of silicon quantum dots using josephson parametric amplification, *Phys. Rev. Lett.* **124**, 067701 (2020).
 - [7] J. M. Elzerman, R. Hanson, L. H. W. van Beveren, B. Witkamp, L. M. K. Vandersypen, and L. P. Kouwenhoven, Single-shot read-out of an individual electron spin in a quantum dot, *Nature* **430**, 431 (2004).
 - [8] K. Ono, D. Austing, Y. Tokura, and S. Tarucha, Current rectification by pauli exclusion in a weakly coupled double quantum dot system, *Science* **297**, 1313 (2002).

- [9] D. Keith, M. G. House, M. B. Donnelly, T. F. Watson, B. Weber, and M. Y. Simmons, Single-shot spin readout in semiconductors near the shot-noise sensitivity limit, *Phys. Rev. X* **9**, 41003 (2019).
- [10] F. Borjans, X. Mi, and J. Petta, Spin digitizer for high-fidelity readout of a cavity-coupled silicon triple quantum dot, *Phys. Rev. App.* **15**, 044052 (2021).
- [11] J. Z. Blumoff, A. S. Pan, T. E. Keating, R. W. Andrews, D. W. Barnes, T. L. Brecht, E. T. Croke, L. E. Euliss, J. A. Fast, C. A. Jackson, A. M. Jones, J. Kerckhoff, R. K. Lanza, K. Raach, B. J. Thomas, R. Velunta, A. J. Weinstein, T. D. Ladd, K. Eng, M. G. Borselli, A. T. Hunter, and M. T. Rakher, Fast and high-fidelity state preparation and measurement in triple-quantum-dot spin qubits, *PRX Quantum* **3**, 010352 (2022).
- [12] G. A. Oakes, V. N. Ciriano-Tejel, D. F. Wise, M. A. Fogarty, T. Lundberg, C. Lainé, S. Schaal, F. Martins, D. J. Ibberson, L. Hutin, B. Bertrand, N. Stelmashenko, J. W. A. Robinson, L. Ibberson, A. Hashim, I. Siddiqi, A. Lee, M. Vinet, C. G. Smith, J. J. L. Morton, and M. F. Gonzalez-Zalba, Fast high-fidelity single-shot readout of spins in silicon using a single-electron box, *Phys. Rev. X* **13**, 011023 (2023).
- [13] R. Zhao, T. Tanttu, K. Y. Tan, B. Hensen, K. W. Chan, J. C. C. Hwang, R. C. C. Leon, C. H. Yang, W. Gilbert, F. E. Hudson, K. M. Itoh, A. A. Kiselev, T. D. Ladd, A. Morello, A. Laucht, and A. S. Dzurak, Single-spin qubits in isotopically enriched silicon at low magnetic field, *Nat. Commun.* **10**, 5500 (2019).
- [14] M. Urdampilleta, D. J. Niegemann, E. Chanrion, B. Jadot, C. Spence, P.-A. Mortemousque, C. Bäuerle, L. Hutin, B. Bertrand, S. Barraud, R. Maurand, M. Sanquer, X. Jehl, S. D. Franceschi, M. Vinet, and T. Meunier, Gate-based high fidelity spin readout in a CMOS device, *Nat. Nanotechnol.* **14**, 737 (2019).
- [15] D. J. Niegemann, V. El-Homsy, B. Jadot, M. Nurizzo, B. Cardoso-Paz, E. Chanrion, M. Dartiaillh, B. Klemmt, V. Thiney, C. Bäuerle, P.-A. Mortemousque, B. Bertrand, H. Niebojewski, M. Vinet, F. Balestro, T. Meunier, and M. Urdampilleta, Parity and singlet-triplet high-fidelity readout in a silicon double quantum dot at 0.5 K, *PRX Quantum* **3**, 040335 (2022).
- [16] M. A. I. Johnson, M. T. Mkadzik, F. E. Hudson, K. M. Itoh, A. M. Jakob, D. N. Jamieson, A. Dzurak, and A. Morello, Beating the thermal limit of qubit initialization with a bayesian maxwell's demon, *Phys. Rev. X* **12**, 041008 (2022).
- [17] D. Keith, S. K. Gorman, L. Kranz, Y. He, J. G. Keizer, M. A. Broome, and M. Y. Simmons, Benchmarking high fidelity single-shot readout of semiconductor qubits, *New J. Phys.* **21**, 063011 (2019).
- [18] J. Danon and Y. V. Nazarov, Pauli spin blockade in the presence of strong spin-orbit coupling, *Phys. Rev. B* **80**, 041301 (2009).
- [19] S. Nadj-Perge, S. M. Frolov, J. W. W. van Tilburg, J. Danon, Y. V. Nazarov, R. Algra, E. P. A. M. Bakkers, and L. P. Kouwenhoven, Disentangling the effects of spin-orbit and hyperfine interactions on spin blockade, *Phys. Rev. B* **81**, 201305 (2010).
- [20] N. Shaji, C. B. Simmons, M. Thalakulam, L. J. Klein, H. Qin, H. Luo, D. E. Savage, M. G. Lagally, A. J. Rimberg, R. Joynt, M. Friesen, R. H. Blick, S. N. Coppersmith, and M. A. Eriksson, Spin blockade and lifetime-enhanced transport in a few-electron Si/SiGe double quantum dot, *Nat. Phys.* **4**, 540 (2008).
- [21] A. C. Betz, R. Wacquez, M. Vinet, X. Jehl, A. L. Saraiva, M. Sanquer, A. J. Ferguson, and M. F. Gonzalez-Zalba, Dispersively detected pauli spin-blockade in a silicon nanowire field-effect transistor, *Nano Lett.* **15**, 4622 (2015).
- [22] D. Q. Wang, O. Kloch, J.-T. Hung, D. Culcer, I. Farrer, D. A. Ritchie, and A. R. Hamilton, Anisotropic pauli spin blockade of holes in a GaAs double quantum dot, *Nano Lett.* **16**, 7685 (2016).
- [23] V. F. Maisi, A. Hofmann, M. Rössli, J. Basset, C. Reichl, W. Wegscheider, T. Ihn, and K. Ensslin, Spin-orbit coupling at the level of a single electron, *Phys. Rev. Lett.* **116**, 136803 (2016).
- [24] T. Fujita, P. Stano, G. Allison, K. Morimoto, Y. Sato, M. Larsson, J.-H. Park, A. Ludwig, A. D. Wieck, A. Oiwa, and S. Tarucha, Signatures of hyperfine, spin-orbit, and decoherence effects in a pauli spin blockade, *Phys. Rev. Lett.* **117**, 206802 (2016).
- [25] J.-Y. Wang, G.-Y. Huang, S. Huang, J. Xue, D. Pan, J. Zhao, and H. Xu, Anisotropic pauli spin-blockade effect and spin-orbit interaction field in an InAs nanowire double quantum dot, *Nano Lett.* **18**, 4741 (2018).
- [26] H. Watzinger, J. Kukučka, L. Vukušić, F. Gao, T. Wang, F. Schäffler, J.-J. Zhang, and G. Katsaros, A germanium hole spin qubit, *Nat. Commun.* **9**, 3902 (2018).
- [27] D. Jirovec, A. Hofmann, A. Ballabio, P. M. Mutter, G. Tavani, M. Botifoll, A. Crippa, J. Kukučka, O. Sagi, F. Martins, J. Saez-Mollejo, I. Prieto, M. Borovkov, J. Arbiol, D. Chrastina, G. Isella, and G. Katsaros, A singlet-triplet hole spin qubit in planar Ge, *Nat. Mater.* **20**, 1106 (2021).
- [28] F. De Palma, F. Oppliger, W. Jang, S. Bosco, M. Janík, S. Calcaterra, G. Katsaros, G. Isella, D. Loss, and P. Scarlino, Strong hole-photon coupling in planar ge for probing charge degree and strongly correlated states, *Nature Communications* **15**, 10.1038/s41467-024-54520-7 (2024).
- [29] F. Borsoi, N. W. Hendrickx, V. John, M. Meyer, S. Motz, F. van Riggelen, A. Sammak, S. L. de Snoo, G. Scappucci, and M. Veldhorst, Shared control of a 16 semiconductor quantum dot crossbar array, *Nat. Nanotechnol.* **19**, 21 (2024).
- [30] R. Li, F. E. Hudson, A. S. Dzurak, and A. R. Hamilton, Pauli spin blockade of heavy holes in a silicon double quantum dot, *Nano Lett.* **15**, 7314 (2015).
- [31] L. C. Camenzind, S. Geyer, A. Fuhrer, R. J. Warburton, D. M. Zumbühl, and A. V. Kuhlmann, A hole spin qubit in a fin field-effect transistor above 4 kelvin, *Nat. Electron.* **5**, 178 (2022).
- [32] L. Peri, F.-E. von Horstig, S. Barraud, C. J. B. Ford, M. Benito, and M. F. Gonzalez-Zalba, Polarimetry with spins in the solid state, *Nano Letters* **25**, 9285 (2025).
- [33] R. Maurand, X. Jehl, D. Kotekar-Patil, A. Corna, H. Bohuslavskyi, R. Laviéville, L. Hutin, S. Barraud, M. Vinet, M. Sanquer, and S. De Franceschi, A CMOS silicon spin qubit, *Nat. Commun.* **7**, 13575 EP (2016).
- [34] F. N. M. Froning, L. C. Camenzind, O. A. H. van der Molen, A. Li, E. P. A. M. Bakkers, D. M. Zumbühl, and F. R. Braakman, Ultrafast hole spin qubit with gate-tunable spin-orbit switch functionality, *Nat. Nanotechnol.* **16**, 308 (2021).

- [35] N. Piot, B. Brun, V. Schmitt, S. Zihlmann, V. P. Michal, A. Apra, J. C. Abadillo-Uriel, X. Jehl, B. Bertrand, H. Niebojewski, L. Hutin, M. Vinet, M. Urdampilleta, T. Meunier, Y.-M. Niquet, R. Maurand, and S. D. Franceschi, A single hole spin with enhanced coherence in natural silicon, *Nat. Nanotechnol.* **17**, 1072 (2022).
- [36] J. Schuff, M. J. Carballido, M. Kotzagiannidis, J. C. Calvo, M. Caselli, J. Rawling, D. L. Craig, B. van Straaten, B. Severin, F. Fedele, S. Svab, P. C. Kwon, R. S. Eggli, T. Patlatiuk, N. Korda, D. Zumbühl, and N. Ares, Fully autonomous tuning of a spin qubit (2024), arXiv:2402.03931 [cond-mat.mes-hall].
- [37] M. J. Carballido, S. Svab, R. S. Eggli, T. Patlatiuk, P. C. Kwon, J. Schuff, R. M. Kaiser, L. C. Camenzind, A. Li, N. Ares, E. P. A. M. Bakkers, S. Bosco, J. C. Egues, D. Loss, and D. M. Zumbühl, Compromise-free scaling of qubit speed and coherence (2024), arXiv:2402.07313 [cond-mat.mes-hall].
- [38] N. W. Hendrickx, W. I. L. Lawrie, M. Russ, F. van Riggelen, S. L. de Snoo, R. N. Schouten, A. Sammak, G. Scappucci, and M. Veldhorst, A four-qubit germanium quantum processor, *Nature* **591**, 580 (2021).
- [39] X. Zhang, E. Morozova, M. Rimbach-Russ, D. Jirovec, T.-K. Hsiao, P. C. F. na, C.-A. Wang, S. D. Oosterhout, A. Sammak, G. Scappucci, M. Veldhorst, and L. M. K. Vandersypen, Universal control of four singlet-triplet qubits (2024), arXiv:2312.16101 [cond-mat.mes-hall].
- [40] S. D. Liles, D. J. Halverson, Z. Wang, A. Shamim, R. S. Eggli, I. K. Jin, J. Hillier, K. Kumar, I. Vorreiter, M. J. Rendell, J. Y. Huang, C. C. Escott, F. E. Hudson, W. H. Lim, D. Culcer, A. S. Dzurak, and A. R. Hamilton, A singlet-triplet hole-spin qubit in mos silicon, *Nature Communications* **15**, 10.1038/s41467-024-51902-9 (2024).
- [41] F. Vigneau, F. Fedele, A. Chatterjee, D. Reilly, F. Kuemmeth, M. F. Gonzalez-Zalba, E. Laird, and N. Ares, Probing quantum devices with radio-frequency reflectometry, *Appl. Phys. Rev.* **10**, 021305 (2023).
- [42] A. West, B. Hensen, A. Jouan, T. Tanttu, C.-H. Yang, A. Rossi, M. F. Gonzalez-Zalba, F. Hudson, A. Morello, D. J. Reilly, and A. S. Dzurak, Gate-based single-shot readout of spins in silicon, *Nat. Nanotechnol.* **14**, 437 (2019).
- [43] F.-E. von Horstig, D. J. Ibberson, G. A. Oakes, L. Cochrane, D. F. Wise, N. Stelmashenko, S. Barraud, J. A. Robinson, F. Martins, and M. F. Gonzalez-Zalba, Multimodule microwave assembly for fast readout and charge-noise characterization of silicon quantum dots, *Physical Review Applied* **21**, 10.1103/physrevapplied.21.044016 (2024).
- [44] J. van der Heijden, T. Kobayashi, M. G. House, J. Salfi, S. Barraud, R. Laviéville, M. Y. Simmons, and S. Rogge, Readout and control of the spin-orbit states of two coupled acceptor atoms in a silicon transistor, *Sci. Adv.* **4**, eaat9199 (2018).
- [45] T. Lundberg, J. Li, L. Hutin, B. Bertrand, D. Ibberson, C.-M. Lee, D. Niegemann, M. Urdampilleta, N. Stelmashenko, T. Meunier, J. Robinson, L. Ibberson, M. Vinet, Y.-M. Niquet, and M. Gonzalez-Zalba, Spin quintet in a silicon double quantum dot: Spin blockade and relaxation, *Phys. Rev. X* **10**, 10.1103/PhysRevX.10.041010 (2020).
- [46] T. Lundberg, D. J. Ibberson, J. Li, L. Hutin, J. C. Abadillo-Uriel, M. Filippone, B. Bertrand, A. Nunnenkamp, C.-M. Lee, N. Stelmashenko, J. W. A. Robinson, M. Vinet, L. Ibberson, Y.-M. Niquet, and M. F. Gonzalez-Zalba, Non-symmetric pauli spin blockade in a silicon double quantum dot, *npj Quantum Inf.* **10**, 1 (2024).
- [47] R. Mizuta, R. M. Otxoa, A. C. Betz, and M. F. Gonzalez-Zalba, Quantum and tunneling capacitance in charge and spin qubits, *Phys. Rev. B* **95**, 045414 (2017).
- [48] We define the g -factor at a particular magnetic field angle as $g = |\mathbf{g}\vec{B}|/|\vec{B}|$ where \mathbf{g} is the g -tensor.
- [49] A. E. Seedhouse, T. Tanttu, R. C. Leon, R. Zhao, K. Y. Tan, B. Hensen, F. E. Hudson, K. M. Itoh, J. Yoneda, C. H. Yang, A. Morello, A. Laucht, S. N. Coppersmith, A. Saraiva, and A. S. Dzurak, Pauli blockade in silicon quantum dots with spin-orbit control, *PRX Quantum* **2**, 010303 (2021).
- [50] M. Urdampilleta, A. Chatterjee, C. C. Lo, T. Kobayashi, J. Mansir, S. Barraud, A. C. Betz, S. Rogge, M. F. Gonzalez-Zalba, and J. J. L. Morton, Charge dynamics and spin blockade in a hybrid double quantum dot in silicon, *Phys. Rev. X* **5**, 031024 (2015).
- [51] G. Burkard, T. D. Ladd, A. Pan, J. M. Nichol, and J. R. Petta, Semiconductor spin qubits, *Rev. Mod. Phys.* **95**, 025003 (2023).
- [52] P. Harvey-Collard, N. T. Jacobson, M. Rudolph, J. Dominguez, G. A. Ten Eyck, J. R. Wendt, T. Pluym, J. K. Gamble, M. P. Lilly, M. Pioro-Ladrière, and M. S. Carroll, Coherent coupling between a quantum dot and a donor in silicon, *Nature Communications* **8**, 1029 (2017).
- [53] A. J. Weinstein, M. D. Reed, A. M. Jones, R. W. Andrews, D. Barnes, J. Z. Blumoff, L. E. Euliss, K. Eng, B. H. Fong, S. D. Ha, D. R. Hulbert, C. A. C. Jackson, M. Jura, T. E. Keating, J. Kerckhoff, A. A. Kiselev, J. Matten, G. Sabbir, A. Smith, J. Wright, M. T. Rakher, T. D. Ladd, and M. G. Borselli, Universal logic with encoded spin qubits in silicon, *Nature* **615**, 817 (2023).
- [54] M. Nurizzo, B. Jadot, P.-A. Mortemousque, V. Thiney, E. Chanrion, D. Niegemann, M. Dartiaill, A. Ludwig, A. D. Wieck, C. Bäuerle, M. Urdampilleta, and T. Meunier, Complete readout of two-electron spin states in a double quantum dot, *PRX Quantum* **4**, 010329 (2023).
- [55] S. G. J. Philips, M. T. Madzik, S. V. Amitonov, S. L. de Snoo, M. Russ, N. Kalhor, C. Volk, W. I. L. Lawrie, D. Brousse, L. Tryputen, B. P. Wuetz, A. Sammak, M. Veldhorst, G. Scappucci, and L. M. K. Vandersypen, Universal control of a six-qubit quantum processor in silicon, *Nature* **609**, 919 (2022).

Supplementary - Electrical readout of spins in the absence of spin blockade

Felix-Ekkehard von Horstig,^{1,2,*} Lorenzo Peri,^{1,3} Virginia N. Ciriano-Tejel,¹ Sylvain Barraud,⁴ Jason A. W. Robinson,² Monica Benito,⁵ Frederico Martins,⁶ and M. Fernando Gonzalez-Zalba^{1,†}

¹Quantum Motion, 9 Sterling Way, London, N7 9HJ, United Kingdom

²Department of Materials Sciences and Metallurgy, University of Cambridge, Charles Babbage Rd, Cambridge CB3 0FS, United Kingdom

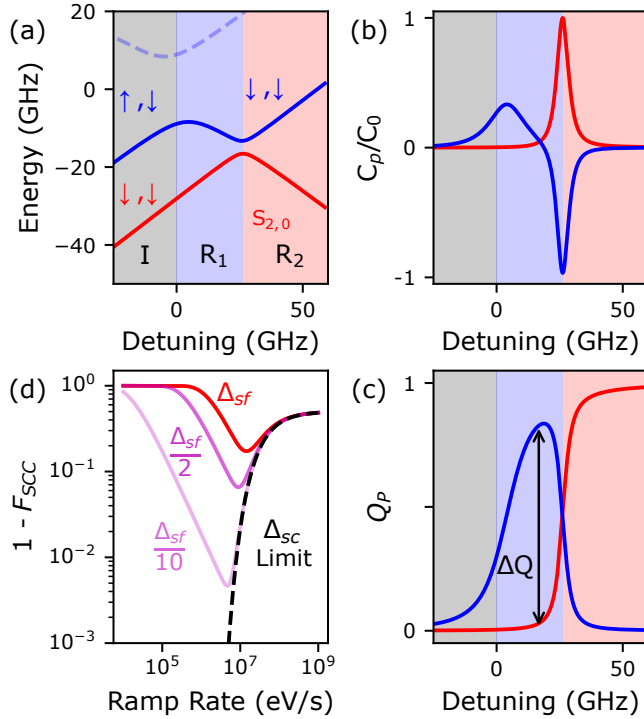
³Cavendish Laboratory, University of Cambridge, JJ Thomson Ave, Cambridge CB3 0HE, United Kingdom

⁴CEA, LETI, Minatec Campus, F-38054 Grenoble, France

⁵Institute of Physics, University of Augsburg, 86159 Augsburg, Germany

⁶Hitachi Cambridge Laboratory, J.J. Thomson Avenue, CB3 0HE, United Kingdom

(Dated: October 9, 2025)



Supplementary Figure 1. Comparison of charge-sensed SB and dispersive sensing. (a) Energy-level diagram of the system in Section ??, showing the initialisation and operation regime (grey), and two potential readout regimes for SB measured via charge sensing (blue and red areas). (b-c) Capacitance C_p (i.e. polarisability) and charge polarisation Q_p plotted against detuning for the parameters plotted in (a). (d) Limitations in F_{SCC} based on incomplete adiabatic transitions when measuring in readout regime R_2 , calculated for the parameters in (a) plotted in solid red and for those with Δ_{sf} reduced by a factor of 2 and 10 in the shaded lines.

Supplementary Note 1: Spin-to-charge conversion fidelity in charge-sensed SB

In charge-sensed SB, the spin system is ramped from within the (1,1) (grey area marked I in Supplementary Figure 1a) into the (2,0) charge configuration (red area marked R_2). In systems with negligible SOC (i.e. Δ_{sf} , $\delta g = 0$), this process is typically performed using a single slow, adiabatic passage (SAP) across the charge anticrossing (i.e. $S_{1,1}/S_{2,0}$) which converts the singlet population into the (2,0) charge configuration, while keeping the triplets in the (1,1) [1]. In the presence of Δ_{sf} , additionally, a fast ramp across the $T_{1,1}/S_{2,0}$ anticrossing may diabatically transition the system into the typical states (i.e. map the $T_{1,1}$ to a (1,1) and the (\uparrow, \downarrow) into the (2,0) charge configuration). Such ramp must be sufficiently large to achieve a diabatic transition with high probability and hence a high spin-to-charge conversion fidelity, F_{SCC} . It is worth highlighting that any loss of fidelity caused by this state projection correspond to errors in the SCC mechanism, which limit the fidelity independently of the sensor's SNR and system's T_1 .

Physical limitations in the maximum achievable ramp rate may place an upper limit on the diabatic transfer fidelity. Based on a 1 V pulse over 1 ns attenuated by 30 dB, with a $\Delta\alpha$ of 0.26, we estimate that the maximum achievable pulse rate in our system is 8.2 MeV/s, limiting the fidelity to diabatically cross the $\uparrow, \downarrow/S_{2,0}$ anticrossing to below 79%. However, even if a faster ramp rate (compared to Δ_{sf}) is achievable, it must also be kept low enough so as not to diabatically excite the states across the $\uparrow, \downarrow/S_{2,0}$ anticrossing, which incorrectly maps the (\uparrow, \downarrow) into the (1,1) charge configuration, therefore reducing F_{SCC} .

For the charge-sensed mode of operation, F_{SCC} is then simply the probability of neither process producing an incorrect spin-to-charge mapping [2], which for a constant ramp rate ν is given by:

$$F_{SCC} = e^{-2\pi \frac{\Delta_{sf}^2}{\hbar\nu}} \left(1 - \frac{1}{2} e^{-4\pi \frac{\Delta_{sc}^2}{\hbar\nu}} \right), \quad (1)$$

Note that by modulating ν it may be possible to achieve

* felix@quantummotion.tech

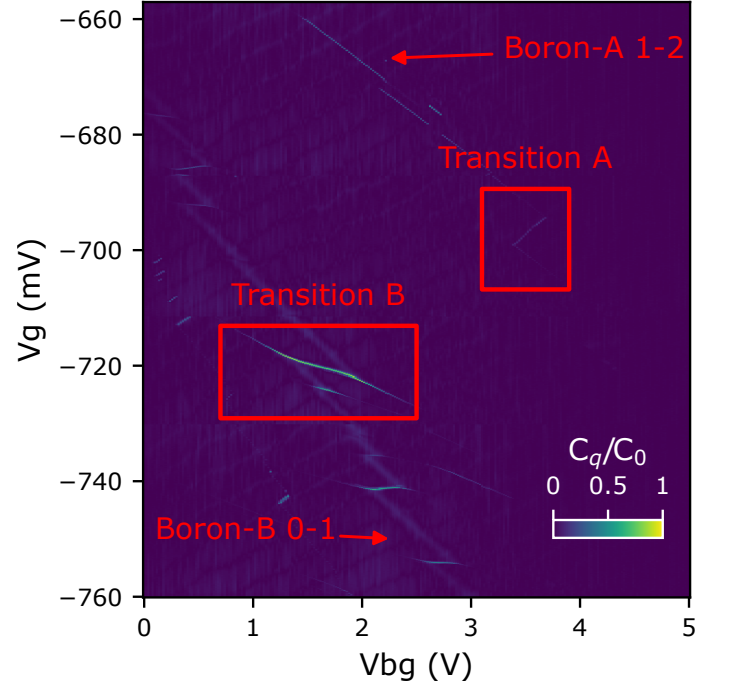
† fernando@quantummotion.tech

an improved F_{SCC} but nevertheless the figure calculated from Eq. 1 can be used as an indication of the limitation imposed by needing to adiabatically transition the spin conserving and diabatically transitioning the spin-flip transition. Additionally, for large Δ_{sf}/Δ_{sc} , finding an optimal ramp sequence may not be trivial at every magnetic field given the potential anticrossing overlap of the Δ_{sf} and Δ_{sc} anticrossings.

For the parameters of Δ_{sf} and Δ_{sc} described in Section ??, we plot the infidelity as a function of ν in Supplementary Figure 1b (dark red trace). At low ν , the fidelity is limited by the probability to cross the Δ_{sf} anticrossing, while at high ν the fidelity is limited by the Δ_{sc} anticrossing (black-dashed line). For the experimental parameters, a maximum fidelity of 68 % can be achieved at the optimal ramp rate of 7 MeV/s. A reduction in Δ_{sf} , which may be achieved by tuning the magnetic field angle [3], can increase the fidelity as demonstrated by the additional, shaded magenta lines in Supplementary Figure 1d for a reduction of Δ_{sf} by a factor of 2 and 10 respectively. It is worth noting that any Δ_{sf} , regardless of how small, will result in a finite infidelity $1-F_{SCC}$, limiting the maximum achievable fidelity by this method of diabatically ramping across the $\downarrow, \downarrow/S_{2,0}$ anticrossing using a constant ramp rate.

Two additional modes of operation may be envisioned to get around this issue: (i) performing the measure before the $\downarrow, \downarrow/S_{2,0}$ anticrossing, or (ii) attempting to traverse the entire energy landscape adiabatically.

1. By measuring between the two anticrossings (blue area marked R_1 in Supplementary Figure 1a), the problem of imperfect diabatic transitions can be avoided as only the $(\uparrow, \downarrow)/S_{2,0}$ transition needs to be crossed adiabatically. However, if the anticrossings are not sufficiently separated, readout fidelity may be limited by their overlap. In Supplementary Figure 1c, we plot the charge polarisation Q_p of the two lowest states, corresponding to the average excess charge on the second dot, as a function of detuning. Note that due to the overlap of the anticrossings, the charge polarisation falls short of unity for the \uparrow, \downarrow state, resulting in a reduced contrast to the $T_{1,1}^-$. This overlap also affects dispersively sensed SB (upper panel) but the impact is less severe. We discuss the impact of this overlap further in Supplementary Note 9.
2. Another mode of operation may be envisioned where both anticrossings are crossed adiabatically and a charge sensor measurement is taken in the region marked R_2 in Supplementary Figure 1a. In this case, the $T_{1,1}^-$ is mapped into the $S_{2,0}$ state (i.e. a (2,0) charge configuration), while the \uparrow, \downarrow is mapped into the $T_{1,1}^-$ state (i.e. a (1,1) charge configuration) – all other states, $T_{1,1}^+$ and \downarrow, \uparrow are also mapped into the (1,1) charge configurations. This charge mapping is opposite to the usual SB. In this



Supplementary Figure 2. Stability map showing the relative location of ICT A and B.

case, the state-projection fidelity is limited by state decay occurring during the time it takes to perform the (slow) adiabatic ramp.

Supplementary Note 2: Stability map showing transitions A and B

The stability map of the device under study shows two Boron-reservoir transitions (red arrows) intersected by several Boron-quantum-dot-transitions. The different Boron acceptors and QDs can be distinguished by their different slope with respect to V_{bg} and V_g indicating different gate lever arms α . The charge occupation of the Boron atoms was deduced from the magneto-spectroscopy. Since Boron atoms can hold at most two holes, and the Boron involved in ICT A already contains two, we conclude that the Boron atoms involved in ICT A and B are distinct Boron atoms. This is supported by the difference in slope (different α) and tunnel rate of the two Boron-reservoir transitions.

Supplementary Note 3: Modelling Energy levels and Magneto-spectroscopy

We introduce the following Hamiltonian to simulate the energy level diagrams and magneto-spectroscopy in this work. We consider first two charge islands with occupation (N_L, N_R) occupied by a total of two spins.

In the following, we assume the left dot is singly/not

occupied, while the right dot is singly/doubly occupied. In the presence of SOC, it is easier to describe the (1,1) occupation in the single spins basis ($|\uparrow_l, \uparrow_r\rangle$, $|\downarrow_l, \uparrow_r\rangle$, $|\uparrow_l, \downarrow_r\rangle$, and $|\downarrow_l, \downarrow_r\rangle$). In the (0,2) occupation, we only include the singlet $|S_{0,2}\rangle$ [4]. In this basis, the Hamiltonian of the system can be found in Eq. (3), which is a generalization of Ref. [4, 5]. The Zeeman energies are de-

$$H = \frac{1}{2} \begin{bmatrix} \varepsilon + (g_l + g_r)B & 0 & 0 & 0 \\ 0 & \varepsilon + (-g_l + g_r)B & 0 & 0 \\ 0 & 0 & \varepsilon + (g_l - g_r)B & 0 \\ 0 & 0 & 0 & \varepsilon + (-g_l - g_r)B \\ -\Delta_{sf} & -\Delta_{sc} & \Delta_{sc} & \Delta_{sf} \end{bmatrix} \begin{bmatrix} -\Delta_{sf} \\ -\Delta_{sc} \\ \Delta_{sc} \\ -\varepsilon \end{bmatrix} \quad (3)$$

This Hamiltonian allows us to calculate the energy level diagrams shown in this paper. To simulate the magneto-spectroscopy, we extract the capacitive signal of the ground state arising from the cyclical variations in charge occupations driven by the tone of the resonator. This gives rise to a parametric capacitance (quantum and tunneling capacitance [8]). We neglect contributions by relaxation events giving rise to Sisyphus resistance [9]. The signal arises whenever two states anticross as this allows the resonator to drive differences in the charge occupation of the QDs. For a two level system with tunnel coupling Δ_0 in the slow relaxation limit (negligible tunneling capacitance), this results in a capacitance of:

$$C_p = \frac{(e\alpha)^2}{2} \frac{\Delta_0^2}{[(\varepsilon - \varepsilon_0)^2 + \Delta_0^2]^{3/2}} \chi_c \quad (3)$$

where C_p is the parametric capacitance, α the lever arm, ε_0 the location of the anticrossing in detuning, and χ_c the charge polarisation. It is worth noting that a smaller Δ_0 will result in sharper and brighter transitions (as long as $\Delta_0 > f_r$ [9, 10]). In the limits described, an intuitive understanding of the capacitive signal arising from a given energy level diagram can be gained from the second derivative (i.e. the curvature) of the energy level with detuning arising from the anticrossing of two states [11].

At zero magnetic field, the spin anti-parallel to $S_{0,2}$ anticrossing dominates the ground state of the system and therefore provides the source of the capacitive signal. Once a magnetic field is applied, the $T_{1,1}^-$ state is lowered below the (\uparrow, \downarrow) and (\downarrow, \uparrow) states which for $g_r - g_l \ll \bar{g}$ and $\Delta_{sf} \ll \Delta_{sc}$ can be found analytically as $\varepsilon \gtrsim [\Delta_{sc}^2 - (2\bar{g}\mu_B B)^2] / (4\bar{g}\mu_B B)$, otherwise the solution can be found numerically. Once $2\bar{g}\mu_B B \gtrsim \Delta_{sc}$ this results in the $T_{1,1}^-$ cutting off the anti-parallel to $S_{0,2}$ signal at zero detuning. If $\Delta_{sf} > 0$, the $T_{1,1}^-$ will then anticross with the $S_{0,2}$ giving rise to a new capacitive signal whose centre follows the hyperbolic expression above.

In the presence of an orbital (or valley) excited state

terminated by the two g factors g_l and g_r for the two QDs respectively, while the (1,1) region is connected to the $|S_{0,2}\rangle$ via a spin-conserving (Δ_{sc}) and a spin-flip (Δ_{sf}) tunnel couplings [3], the latter arising from the presence of SOC and thus potentially different spin quantization axes between the left and right QDs [6, 7].

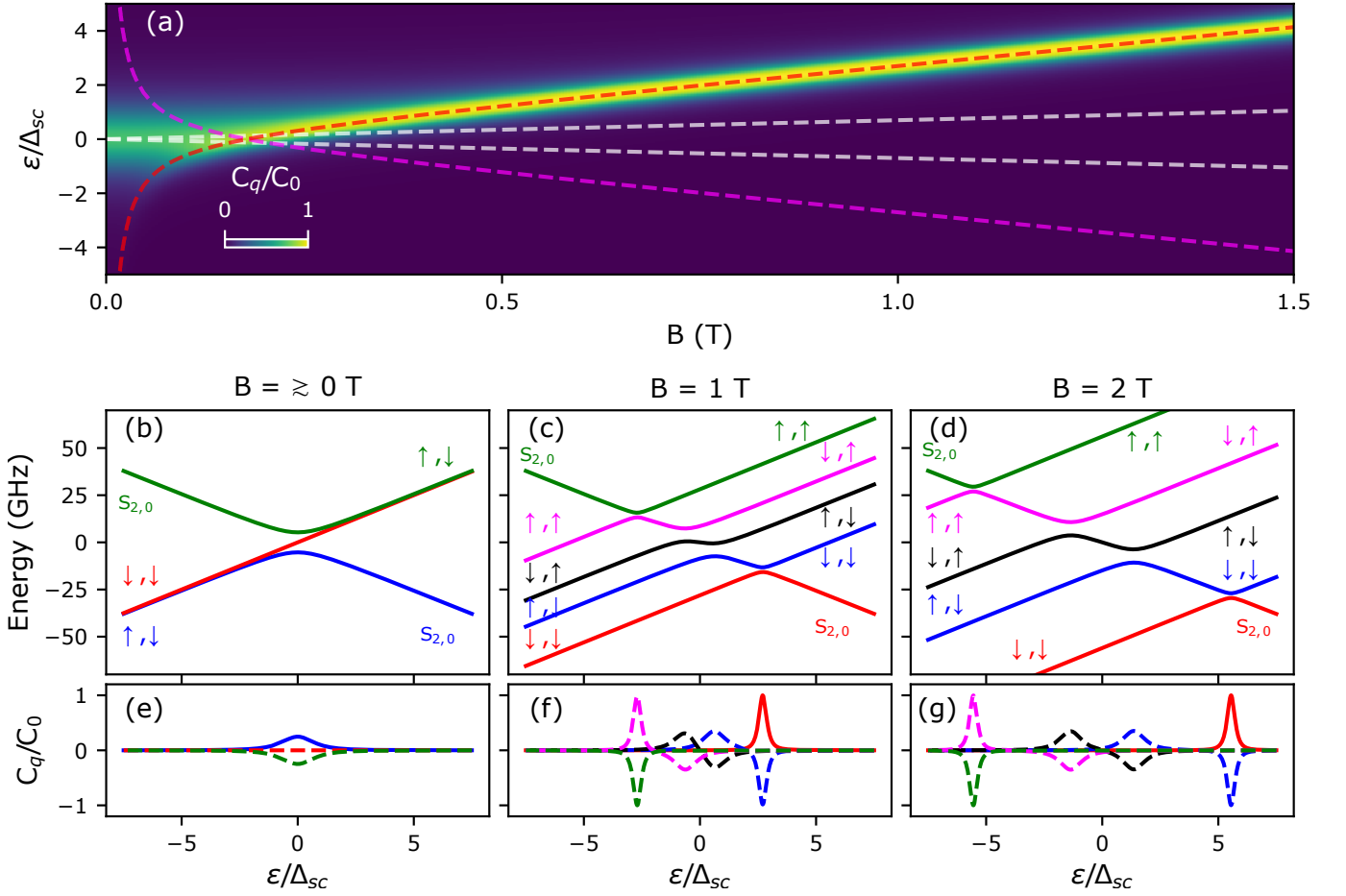
in the right dot (Section ??), separated from the ground state in the right by an energy δ_o , we can extend the model in Eq. (3) to include the state $|T_{0,2}^- \rangle$. Once $2g_r\mu_B B \gtrsim \delta_o$, the $T_{0,2}^-$ is also lowered below the $S_{0,2}$ state. At this point, the ground state anticrossing switches from the $T_{1,1}^-/S_{0,2}$ to the $T_{1,1}^-/T_{0,2}^-$ at $\varepsilon = \delta_o + 1/2 (g_l - g_r)\mu_B B$. For the sake of simplicity of the model, we assume that the overlap of the two states with the left QD are similar enough not to meaningfully alter the tunnel coupling, or the g -factor. Therefore, we assume Δ_{sc} and Δ_{sf} to be the same for both $|S_{0,2}\rangle$ and $|T_{0,2}^- \rangle$, as confirmed by the experimental measurement in Section ??.

Supplementary Note 4: Readout locations for hole and electron systems

In this section, we will discuss how different anticrossings can be used for state readout and the impact of magnetic field on the anticrossing separation of these states. For the purposes of clarity, we will split this section into two regimes: (i) Systems with strong SOC (e.g. hole spins in Si, Ge), resulting in significant Δ_{sf} but where we neglect low-lying orbital states, and (ii) systems with weak SOC (e.g. electrons spins in Si), where $\Delta_{sf} = 0$ and $g_l = g_r$ but low-lying orbital or valley states are taken into account. Holes in QDs can exhibit both SOC and low lying orbital states (not discussed here) leading to a combination of the two effects.

4.1. Readout in systems with strong SOC and full state readout

To discuss the readout points available for systems with strong SOC, we plot a simulated magneto-spectroscopy map, energy level diagrams, and quantum capacitance signals for a DQD system with $\Delta_{sc} = 10$ GHz, $\Delta_{sf} = \Delta_{sc}/4$, and $g_l = 1.5$, $g_r = 2.5$ (Fig. Sup-



Supplementary Figure 3. Readout locations for systems with strong SOC: a) Simulated magneto-spectroscopy of a two spin system with $\Delta_{sf} = 10$ GHz, $\Delta_{sf} = \Delta_{sf}/4$, and $g_l = 1.5$, $g_r = 2.5$. The location of the $T_{1,1}^-/S_{2,0}$, $T_{1,1}^+/S_{2,0}$ anticrossings are marked with dashed lines in red and pink while those for the $(\uparrow, \downarrow)/S_{2,0}$ and $(\downarrow, \uparrow)/S_{2,0}$ are marked in white. b,c,d) Energy level diagrams at $B = 0, 1$ T and 2 T with d,e,f) the quantum capacitance arising from each state states. At elevated magnetic field there are four readout points corresponding to the $T_{1,1}^-$, (\uparrow, \downarrow) , (\downarrow, \uparrow) and $T_{1,1}^+$ states.

plementary Figure 3). In this case, we do not consider orbital excited states.

At elevated magnetic fields, the $T_{1,1}^-$, (\uparrow, \downarrow) , (\downarrow, \uparrow) and $T_{1,1}^+$ each anticross with the $S_{2,0}$ (Supplementary Figure 3d and g), giving rise to four distinct readout points which can be used to perform full state readout. Given a long enough T_1 , combined with slow enough ramp rates to ensure adiabatic passage of the anticrossings ($\hbar\nu \ll \Delta$), the distinct readout points could allow a full characterization of the state of the two spin system in a complementary way to what has been demonstrated in Ref. [12].

The readout sequence for full two-spin state might involve successively adiabatically ramping to all or a subset of the readout points occurring at the anticrossings between each of the spin states and the $S_{2,0}$, and measure the quantum capacitance, C_q , via a resonator response. Note that some of the states will produce C_q responses at multiple readout points: for example the $T_{1,1}^+$ state will produce a positive C_q at the $T_{1,1}^+$ to $S_{0,2}$ anticrossing, but

will produce a negative C_q at the (\downarrow, \uparrow) to $S_{0,2}$ anticrossing. Since the sign of the anticrossing differs however, these cases can be distinguished as they produce an opposite dispersive shift on the resonator.

In the minimal case, a measurement at the (\downarrow, \uparrow) to $S_{0,2}$ anticrossing allows the $T_{1,1}^+$ state (negative C_q) and (\downarrow, \uparrow) state (positive C_q) to be distinguished from each other and from the remaining (\uparrow, \downarrow) and $T_{1,1}^-$ states (no C_q). This could be followed by a measurement at the $T_{1,1}^-$ to $S_{0,2}$ anticrossing which produces a negative C_q for the \uparrow, \downarrow , a positive C_q for the $T_{1,1}^-$, and no C_q for the remaining (\downarrow, \uparrow) and $T_{1,1}^+$ state. Together, these two measurements are able to distinguish the four states from each other.

The ability to subsequently measure the occupation of the states may be used to detect state leakage out of the computational subspace. If between the individual measurement steps, the spin state decays or state leakage out of the computational subspace occurs (e.g. into higher-orbital states or due to the loss or gain of an additional

charge), this error can also be detected by an erroneous response of the measurement protocol. For example, a positive C_q at the first measurement step (indicating a (\downarrow, \uparrow) state) followed by a positive C_q in the second measurement step (indicating a $T_{1,1}^-$ state) could indicate a decay in the second spin. More thorough measurement procedures may be able to detect more or different kinds of errors at the cost of longer measurement time. For example, negative C_q recorded at the $T_{1,1}^+$ to $S_{0,2}$ anticrossing would indicate the spin state had leaked out of the computational subspace into $S_{0,2}$.

To allow for sufficient visibility between the states, the readout locations need to be separated from each other to avoid signal overlap, as was discussed in Supplementary Note 9. This can be done either by changing the tunnel coupling, as discussed before, or by increasing the magnetic field: The T^+/S and T^-/S each move in detuning with magnetic field described by $\varepsilon_{\pm} = \pm [\Delta_c^2 - (2g\mu_B B)^2] / 4g\mu_B B$ (see red and pink dashed lines in Fig. Supplementary Figure 3a). For the anti-aligned states, the separation is determined by the difference in g-factor $\delta g = g_r - g_l$ giving $\varepsilon_{(\uparrow, \downarrow)/(\downarrow, \uparrow)} \approx \pm \delta g \mu_B B / 2$ (white dashed lines).

In order to allow for sufficient fidelity in the adiabatic passage, the ramp rate to transition onto and between the readout locations needs to be sufficiently slow as determined by the Landau-Zener equation. While in principle the time to perform the slow ramps may allow for state decay to occur, the large charge coupling typical of dispersive readout significantly reduces this time. If, for example a detuning range of 100 GHz needs to be crossed with a anticrossing of 1 GHz in the range, a ramp rate of 17.7 keV/s (taking 2.3 μ s) could be used to achieve an infidelity of only 10^{-4} .

4.2. Readout in systems with orbital excited states

Low-lying orbital (or valley) states are common in gate-defined QDs and their effect on the readout positions should be considered. While, it was more appropriate to describe the case of holes in Si in the single spin basis due to their sizable g-factor difference, for electron in Si, where g-factors tend to be isotropic and SOC is weak, it is more practical to use the Singlet-Triplet basis. We define the singlet and unpolarized triplet as $S_{1,1} = (\downarrow, \uparrow - \uparrow, \downarrow) / \sqrt{2}$ and $T_{1,1}^0 = (\downarrow, \uparrow + \uparrow, \downarrow) / \sqrt{2}$, respectively. To provide a complete discussion, we additionally include the three Triplet states in the (0,2) charge occupancy involving the orbital excited state.

We plot a simulated magneto-spectroscopy map, energy level diagrams and quantum capacitance signals for a DQD housing two spins with $\Delta_c = 10$ GHz, $\delta_o = 4\Delta_c$ and $g_l, g_r = 2$ ($\Delta_{sf} = 0$) in Fig. Supplementary Figure 4. The existence of the orbitally excited $T_{0,2}$ states significantly increases the complexity of the energy level diagrams (Fig. Supplementary Figure 3c,d,e). However, the quantum capacitance only arises from a few anticross-

ings: $S_{1,1}/S_{0,2}$, $T_{1,1}^-/T_{0,2}^-$, $T_{1,1}^0/T_{0,2}^0$, $T_{1,1}^+/T_{0,2}^+$, which are marked in blue/green, red/magenta, black/cyan and pink/orange respectively. In principle the three T/T anticrossings shift in magnetic field according to their g-factor difference ($g_l - g_r$) but since we have set all g-factors to be the same (as is typical for electron in Si) this does not occur here. As a result, only two distinct readout locations are present arising from the S/S anticrossing at $\varepsilon = 0$ and from the three T/T anticrossings located at $\varepsilon = \delta_o$ (Fig. Supplementary Figure 4c,d,e). These readout points are present at all magnetic fields, allowing for singlet-triplet readout independent of the magnetic field intensity.

To increase readout visibility, the separation of the readout locations should be maximised. These are fixed with magnetic field in this case. We therefore require the orbital (or valley) energy δ_o to be sufficiently large compared to the tunnel coupling Δ_c . This can be done by either careful engineering of the QDs to result in larger δ_o or by reducing Δ_c via the use of tunnel barrier gates. We note, the methodology described here can also be extended to other QD systems such as readout of spin-charge hybrid qubits [13, 14] where the two states of the computational basis experience distinct anticrossings separated from each other in detuning.

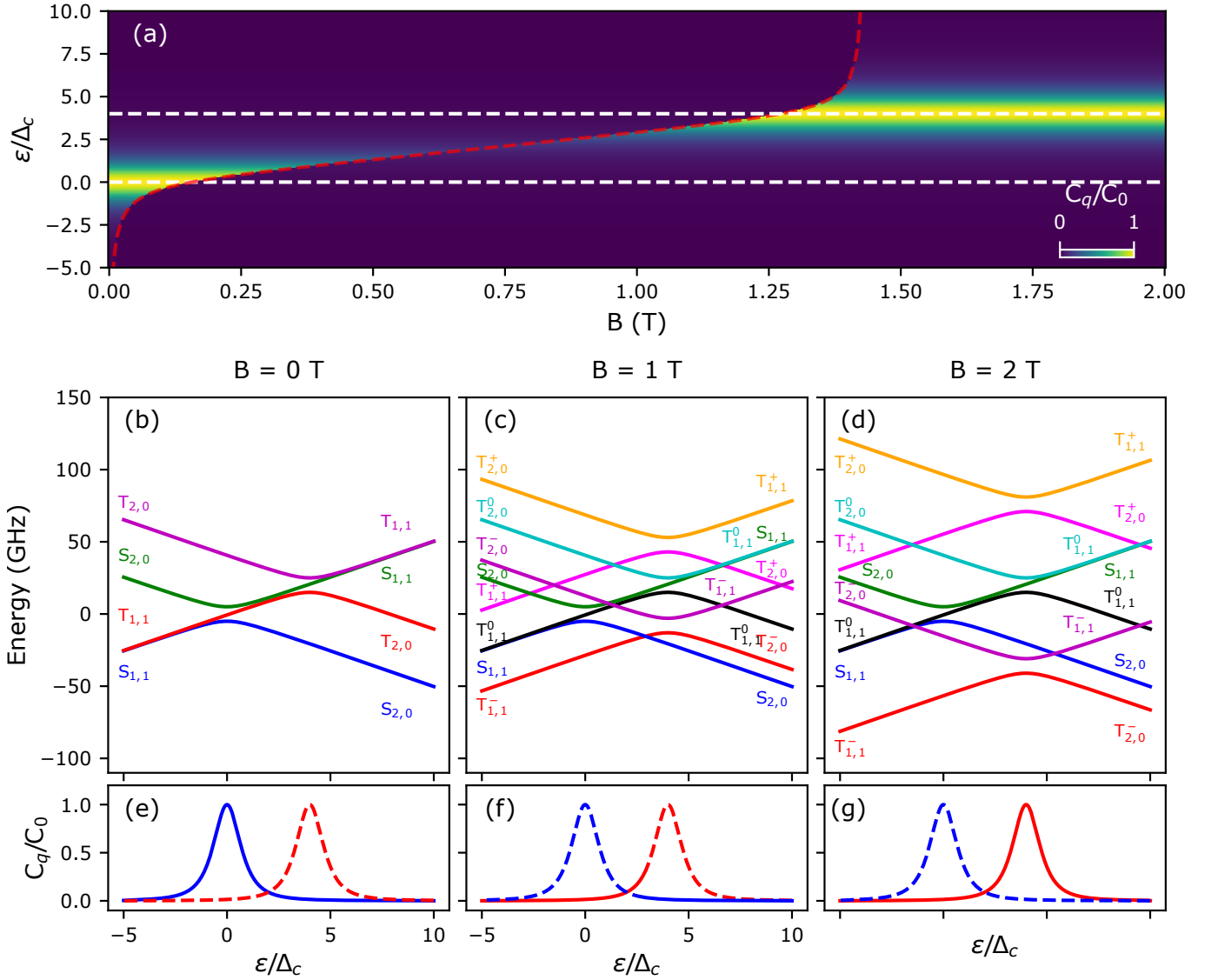
Supplementary Note 5: Multivalued state measurements

As shown in Fig. ??i from the main manuscript, at detuning $\epsilon = 0.1$ meV the quantum capacitance, C_q , takes on different values based on the spin states of the double quantum dot:

- The state $|\downarrow, \downarrow\rangle$ has a negative quantum capacitance.
- The state $|\downarrow, \uparrow\rangle$ has a positive quantum capacitance.
- The states $|\uparrow, \downarrow\rangle$ and $|\uparrow, \uparrow\rangle$ both result in $C_q = 0$.

To readout the spin state, the device is integrated into a resonator (Supplementary Figure 5a) whose impedance response shifts with the value of C_q . Supplementary Figure 5b shows simulated readout data for the three possible C_q values. Each point represents a time-averaged readout trace, and due to noise, points cluster into distinct ‘‘lollipop-like’’ shapes corresponding to the different C_q values. This behaviour is akin to how multi-level qubits in superconducting systems respond [15, 16].

We can classify the resonator response in one of the three states by dividing the signal in the IQ plane into three regions separated by threshold lines. This method is similar to the thresholding approach used in Pauli spin blockade but extends into two dimensions and includes two thresholds to account for the three spin states. Beyond thresholding, more advanced machine learning techniques, such as support vector machines or neural networks, could enhance classification [15, 17].

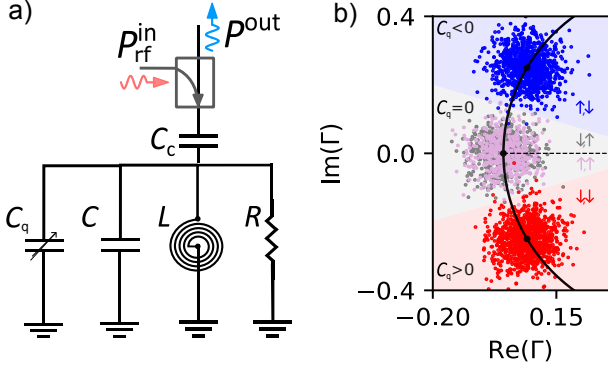


Supplementary Figure 4. Readout locations for systems with orbital excited states: a) Simulated magneto-spectroscopy of an electron double quantum dot with $\Delta_c = 10$ GHz, $\delta_o = 4\Delta_c$ and $g_l, g_r = 2$ ($\Delta_{sf} = 0$). The location of the S/S (left), and T/T (right) anticrossings are marked with white dashed lines, the location of the T⁻/S crossing is marked with a red dashed line. b,c,d) Energy level diagrams at $B = 0, 1$ T and 2 T with e,f,g) the quantum capacitance arising of the $S_{1,1}$ and $T_{1,1}$ states. In each case the capacitance arising from the instantaneous ground state is plotted in a solid line, while excited states are plotted in dashed lines. There are two readout points corresponding to the $S_{1,1}$ and $T_{1,1}$ outcomes.

For a reliable assessment of classification performance in this *tri-state* setup, the standard concept of state fidelity must be slightly modified. Borrowing from machine learning, the magnitude *recall* is introduced to measure the classification accuracy for each state independently: recall for a specific state is defined as 1 - (misclassified traces for that state / total traces for that state). Additionally, the visibility of the readout remains defined as in the classical two-state scenario, capturing overall readout accuracy as 1 - (total errors / total measurements).

Supplementary Note 6: T⁻/S anticrossing detuning dependence with Magnetic field

To further characterise the behaviour of the readout in the T⁻/S coupled regime of ICT A, we characterise the location of the excited (\uparrow_B, \downarrow_D)/S anticrossing as a function of magnetic field. We carry out readout experiments like those described in section ?? and measure the separation of the ground state signal arising from the T⁻/S anticrossing from the excited state signal arising from the (\uparrow_B, \downarrow_D)/S anticrossing (Fig. Supplementary Figure 6a-c). We find this dependency to be approximately linear, with a slope given by $\Delta\epsilon = \hat{g}\mu_B B$ from which we



Supplementary Figure 5. a) Lumped element schematic of the resonator whose device capacitance, ΔC_q , depends on the spin state of the DQD. b) Impedance of a perfectly matched resonator as a function of frequency in the Smith chart (black circle). At the resonant frequency the resonator impedance ideally reaches the origin point (0,0). The three distinct clusters represent the simulated time-averaged impedance response of the resonator under three conditions: $\Delta C_q = 0$ (grey/pink), $\Delta C_q > 0$ (red) and $\Delta C_q < 0$ (blue). The three states can be classified by dividing the Smith chart into three regions, where each region corresponds to a different spin state.

extract \bar{g} of $2.01 \pm .08$, in line with what was extracted from magneto-spectroscopy (Fig. Supplementary Figure 6d,e).

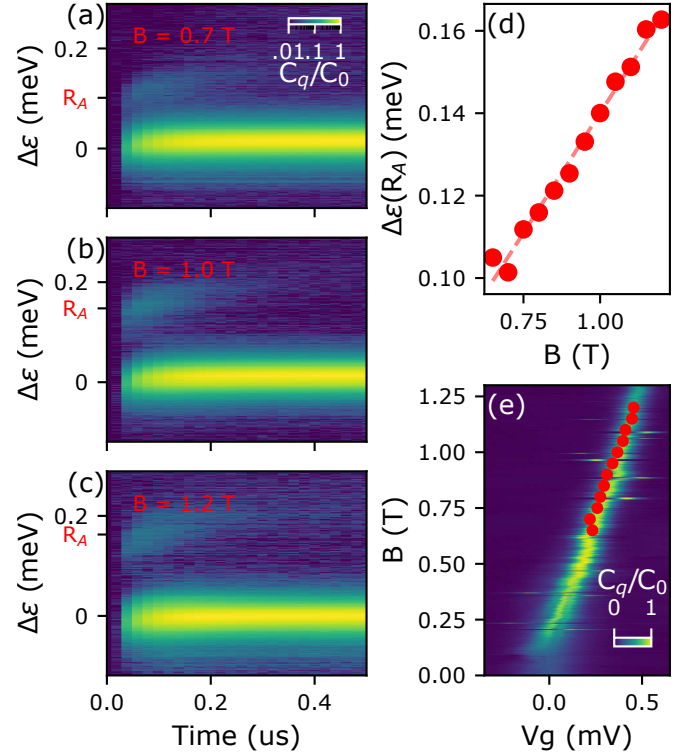
Supplementary Note 7: Improvements required for single shot readout beyond the fault tolerance threshold

For practical quantum computing, qubit readout with a fidelity exceeding the error-correction threshold, e.g. about 99% for the surface code [18], must be achieved. To estimate the requirements for such fidelity, we shall inspect the equation for the readout fidelity assuming simple box-car integration [19, 20]:

$$F = \text{erf} \left[\sqrt{\frac{t_{\text{int}}}{2t_{\text{min}}}} \right] e^{-\frac{t_{\text{int}}}{2T_1}}, \quad (7)$$

where $\text{erf}(x)$ is the error function, t_{int} is the integration time, and t_{min} is the minimum integration time which is a measure of the electrical sensitivity of the measurement apparatus, defined as the integration time where the signal-to-noise ratio (SNR) is unity. We use here the fidelity as defined by Ref. [19] where the fidelity is defined between 0 and 1. Note that this equation does not take into account the finite bandwidth of the readout resonator, which could lead to a lower fidelity at low t_{int} due to the resonator ring-up.

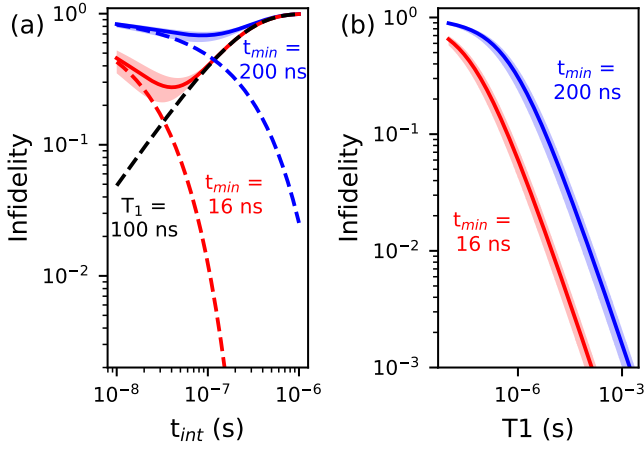
Equation 7 describes two opposing factors that impact fidelity: increasing t_{int} results in an improved electrical



Supplementary Figure 6. Characterisation of Readout point location for spin-orbit lifted readout against magnetic field: (a-c) Capacitive signal vs readout time like that in Fig. ??d at three different fields. Note that the short-lived excited state signal (marked with R_A) shifts with respect to the long-lived ground state signal. (d) Center of excited state signal location relative to the ground state signal as a function magnetic field. The dashed line has a slope of $\partial\epsilon/\partial B = \bar{g}\mu_B$ with \bar{g} of $2.01 \pm .08$. (e) The line in d overlaid on the magneto-spectroscopy data shown in Fig. ??d showing a good match.

SNR with a rate determined by t_{min} , but also increases the probability of relaxation of the state occurring during the measurement time, with a rate determined by T_1 . This leads to an optimum t_{int} which can be found given a t_{min} and T_1 , see Supplementary Figure 7. To improve fidelity, one must therefore improve these two metrics.

First, we estimate t_{min} for the measurements in Fig. ?? d (see Supplementary Note 8) and find t_{min} is 200 ± 80 ns and 16 ± 6 ns for the $(\uparrow_B, \downarrow_D) - S_{2,0}$ and the $(\downarrow_B, \downarrow_D) - S_{2,0}$ transitions, respectively. We attribute the large difference in t_{min} to the lower tunnel coupling. Particularly, $\Delta_{\text{sf}} \sim 3.4$ GHz approaches the resonator frequency of 2.1 GHz which maximises the resonator response [8, 10]. While our system lacked control of the tunnel coupling, Δ_{sc} could be optimised to improve the readout time. Further improvements in t_{min} may be achieved by improved resonator design, for example by increasing the frequency, internal quality factor or the fractional change in capacitance [21]. The use of quantum-limited amplifiers such as Josephson parametric amplifiers (JPAs) or kinetic inductance parametric amplifiers (KIPAs) could further reduce the noise temper-



Supplementary Figure 7. Readout fidelity as a function of t_{int} , t_{min} and T_1 as calculated by Eq. 7. (a) In-fidelity against t_{int} calculated using the experimental values of t_{min} and T_1 . The plot shows optima where errors from T_1 and insufficient SNR balance. (b) Optimum Fidelity achievable as a function of T_1 for $t_{\text{min}} = 200$ ns (blue) and 16 ns (red). The shaded areas represents the uncertainty the infidelity due to the uncertainty in the measured t_{min} .

ature compared to that of the cryogenic high-electron-mobility transistor (HEMT) amplifier used in this experiment ($T_{n,\text{HEMT}} \sim 2.5$ K) by up to an order of magnitude [22]. To estimate the effect such improvements may have, we compare our measurements to the state-of-the-art in dispersive charge sensing performed using a high-frequency resonator and a JPA [23]. Adjusting for the impact of the lever arm on readout signal using the load-aware metric $t_{\text{min}}\alpha^2$ [24], we arrive at a representative t_{min} of 2.4 ns.

Next, we discuss the impact of T_1 . In the present setup, readout fidelity is limited by the state decay due to a short T_1 at the readout point on the order of 100 ns, preventing single-shot readout. We hypothesize that the short T_1 at the readout point is caused by the strong spin-orbit coupling in our sample that enables charge noise to couple into the spin degrees of freedom [25]. This is supported by the exponential dependence of T_1 with detuning away from the anticrossing (Fig. ??), where the spin-carrying charges have the largest dipole and therefore are most impacted by charge noise. Further, although a detailed study of this was not carried out, the T_1 at the readout point shows no significant dependence with magnetic field – see data presented in Supplementary Note 6. This indicates that T_1 is likely not limited by phonon-mediated decay ($1/T_1 \propto B^7$) or due to fixed external magnetic field gradient or hyperfine-induced relaxation (both $1/T_1 \propto B^5$) [25]. To reduce charge noise, improvements in the fabrication of the nanowire transistor could be of help, such as replacing the high- κ gate dielectric, which is known to produce excessive charge noise [26], with SiO₂.

In Supplementary Figure 7b, we plot the measurement

infidelity ($1 - F$) at the optimum t_{int} as a function T_1 for $t_{\text{min}} = 200$ ns and 16 ns. Extracting the required T_1 to achieve a fidelity of 99%, we arrive at 120 ± 50 μ s, 9.5 ± 3 μ s and, for the extrapolation of $t_{\text{min}} = 2.4$ ns from Ref. [23], 1.4 μ s. While these T_1 are significantly longer than what was measured in this system, they are on the order of or lower than T_1 measured in spin systems measured using direct dispersive methods [27] as well as hole spin systems [28–30].

Supplementary Note 8: Estimation of minimum measurement time.

We estimate t_{min} from the data in the magneto-spectroscopy in ?? using the SNR of the resonator response. Extrapolating using a white noise model, this is given by [21]

$$t_{\text{min}} = t_{NE}/\text{SNR}^2, \quad (8)$$

where the SNR is calculated from the peak amplitude over the noise, taken as the standard deviation of the signal at far detuning, and t_{NE} is the noise equivalent integration time given by

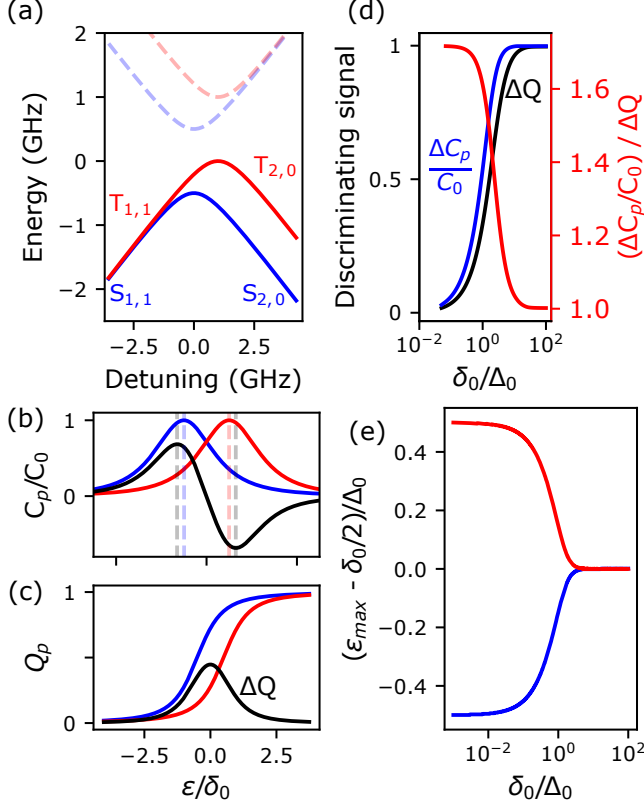
$$t_{NE} = n_{\text{avg}}/2\Delta f, \quad (8)$$

which takes into account the number of averages ($n_{\text{avg}} = 200$ in the magneto-spectroscopy dataset), as well as the equivalent noise bandwidth ($\Delta f = 1.57f_c$ for a single-node low-pass filter with cut-of frequency $f_c = 30$ kHz in this case), resulting in t_{NE} of approximately 2.13 ms. Note that the long integration time is likely to introduce a reduction in the SNR due to charge noise [24], meaning the true t_{min} is likely to be lower.

Using this method for the data in Fig. ?? d, we estimate the t_{min} for the response of the (\uparrow_B, \downarrow_D) - $S_{2,0}$ and the ($\downarrow_B, \downarrow_D$) - $S_{2,0}$ transitions by sampling the extrapolated t_{min} at magnetic fields below 50 mT and at magnetic fields above 600 mT respectively, which ensures that the resonator response purely arises from the desired states. For these anticrossings, the resulting t_{min} is 200 ± 80 ns and 16 ± 6 ns respectively. The large errors arise due to the extrapolation to low integration times from a single point.

Supplementary Note 9: Impact of anticrossing overlap on dispersive and charge sensed readout visibility

As discussed in Supplementary Note 1 and represented in Supplementary Figure 8 b and c, an overlap in detuning of the relevant spin produces a loss of signal contrast for both charge-sensed and dispersive readout. This overlap impacts, for example, the signal contrast in the



Supplementary Figure 8. Comparison of impact of anticrossing overlap for charge sensed SB and dispersive sensing. (a) Energy-level diagram an orbitally lifted with $\Delta_{sc} = \delta_0 = 1$ GHz. (b, c) Capacitance C_p (i.e. polarisability) and charge polarisation Q_p plotted against detuning for the parameters plotted in (a). The $S_{1,1}$ and $S_{0,2}$, and $T_{1,1}/T_{0,2}$ states are plotted in blue and red respectively. The black lines show the signal contrast of ΔC_p and ΔQ_p . (d) Maximum ΔC_p and ΔQ , as well as their normalised ratio plotted against orbital energy δ_0 . (e) Detuning-location of maximum ΔC_p plotted as offset from the bare anticrossing location, as a function of anticrossing separation δ_0 .

experiment in Section ???. In this Supplementary, we shall quantify the impact of signal loss as a function of anticrossing separation for both dispersive readout and conventional charge-sensed SB, see Fig Supplementary Figure 8d-e.

For the sake of simplicity, we examine the case of an orbitally lifted SB at high magnetic field (so the $(\downarrow, \downarrow)/S_{2,0}$ anticrossing can be ignored), where the orbital states are separated by energy δ_0 and we have $\Delta_{sf} = 0$ and $\Delta_{sc} =$

Δ_0 . This produces two anticrossings for the \downarrow, \downarrow and \uparrow, \downarrow states with equal coupling to their respective $(0,2)$ states, separated by δ_0 , which we can then adjust to evaluate the impact of the separation of the anticrossings. Note that a similar approach may be taken to evaluate the impact in the spin-orbit lifted SB case.

In Supplementary Figure 8b-c, we plot the normalized capacitance C_p/C_0 (b) and the charge polarization Q_p (c) for the \uparrow, \downarrow and \downarrow, \downarrow states (blue and red solid lines) as a function of reduced detuning for the case $\delta_0 = \Delta_0$. Furthermore, we plot the signal contrast ΔC_p and ΔQ_p (solid black lines). Note that in the upper panel for C_p , both the maximum signal contrast amplitude ($|\Delta C_p|/C_0$), and the detuning location at which it occurs (ϵ_{max} , vertical black dashed lines) differ from that of the pure signal (vertical blue and red dashed lines).

In Supplementary Figure 8d, we vary δ_0 and plot the maximum signal contrast of $|\Delta C_p|/C_0$ (blue) and ΔQ_p (black). We also plot the ratio of the signal contrasts for the two cases (red). In either case, a signal reduction occurs when δ_0 is of the order of Δ_0 . However, while both cases are affected, $|\Delta C_p|/C_0$ is more resilient, as shown by the red line. This difference originates from the fact that, unlike the dispersive case, the optimum readout location for the charge-sensed case is located at the midpoint of the anticrossings, increasing the impact of the overlap.

For the dispersive case, the location at which the maximum ΔC_p occurs is a function of δ_0 as shown in Supplementary Figure 8e. When δ_0 becomes of the order of Δ_0 , the ϵ_{max} for the two states are pushed outward, plateauing at a value of δ_0 for $\delta_0/\Delta_0 \ll 1$ (ie ϵ_{max} becomes entirely determined by δ_0). These results highlight the importance of calibrating the readout points for low-energy anticrossing separations.

To improve δ_0/Δ_0 , two general approaches can be taken: (i) in the spin-orbit case, the magnetic field can be adjusted to increase the separation δ_0 of the \uparrow, \uparrow and \downarrow, \uparrow anticrossings with $S_{2,0}$. (ii) Tunnel barriers (if present) can be used to decrease tunnel coupling Δ_0 which increases the ratio of δ_0/Δ_0 . With the latter approach, care should be taken not to reduce the Δ of the state to be measured below the resonator frequency f_r when utilizing gate dispersive readout, as this reduces the signal amplitude [10]. A detailed description of the various readout points and their separations for the two systems described in this work can be found in Supplementary Note 4.

-
- [1] J. M. Taylor, J. R. Petta, A. C. Johnson, A. Yacoby, C. M. Marcus, and M. D. Lukin, Relaxation, dephasing, and quantum control of electron spins in double quantum dots, Phys. Rev. B **76**, 035315 (2007).
 [2] L. Peri, F.-E. von Horstig, S. Barraud, C. J. B. Ford,

- M. Benito, and M. F. Gonzalez-Zalba, Polarimetry with spins in the solid state, Nano Letters **25**, 9285 (2025).
 [3] C. X. Yu, S. Zihlmann, J. C. Abadillo-Uriel, V. P. Michal, N. Rambal, H. Niebojewski, T. Bedecarrats, M. Vinet, É. Dumur, M. Filippone, B. Bertrand, S. De Franceschi,

- Y.-M. Niquet, and R. Maurand, Strong coupling between a photon and a hole spin in silicon, *Nat. Nanotechnol.* **18**, 741 (2023).
- [4] M. Veldhorst, C. H. Yang, J. C. C. Hwang, W. Huang, J. P. Dehollain, J. T. Muhonen, S. Simmons, A. Laucht, F. E. Hudson, K. M. Itoh, A. Morello, and A. S. Dzurak, A two-qubit logic gate in silicon, *Nature* **526**, 410 (2015).
- [5] J. Danon and Y. V. Nazarov, Pauli spin blockade in the presence of strong spin-orbit coupling, *Phys. Rev. B* **80**, 041301 (2009).
- [6] A. Sen, G. Frank, B. Kolok, J. Danon, and A. Pályi, Classification and magic magnetic field directions for spin-orbit-coupled double quantum dots, *Physical Review B* **108**, 10.1103/physrevb.108.245406 (2023).
- [7] F. van Riggelen-Doelman, C.-A. Wang, S. L. de Snoo, W. I. L. Lawrie, N. W. Hendrickx, M. Rimbach-Russ, A. Sammak, G. Scappucci, C. Déprez, and M. Veldhorst, Coherent spin qubit shuttling through germanium quantum dots, *Nature Communications* **15**, 10.1038/s41467-024-49358-y (2024).
- [8] R. Mizuta, R. M. Otxoa, A. C. Betz, and M. F. Gonzalez-Zalba, Quantum and tunneling capacitance in charge and spin qubits, *Phys. Rev. B* **95**, 045414 (2017).
- [9] M. Esterli, R. M. Otxoa, and M. F. Gonzalez-Zalba, Small-signal equivalent circuit for double quantum dots at low-frequencies, *Appl. Phys. Lett.* **114**, 253505 (2019).
- [10] L. Peri, M. Benito, C. J. B. Ford, and M. F. Gonzalez-Zalba, Unified linear response theory of quantum electronic circuits, *npj Quantum Information* **10**, 114 (2024).
- [11] K. D. Petersson, C. G. Smith, D. Anderson, P. Atkinson, G. A. C. Jones, and D. A. Ritchie, Charge and spin state readout of a double quantum dot coupled to a resonator, *Nano Lett.* **10**, 2789 (2010).
- [12] M. Nurizzo, B. Jadot, P.-A. Mortemousque, V. Thiney, E. Chanrion, D. Niegemann, M. Dartiailh, A. Ludwig, A. D. Wieck, C. Bäuerle, M. Urdampilleta, and T. Meunier, Complete readout of two-electron spin states in a double quantum dot, *PRX Quantum* **4**, 010329 (2023).
- [13] D. Kim, C. Simmons, D. Ward, J. Prance, T. S. Koh, J. King Gamble, D. Savage, M. Lagally, M. Friesen, S. Coppersmith, and M. Eriksson, Quantum control and process tomography of a semiconductor quantum dot hybrid, *Nature* **511**, 70 (2014).
- [14] W. Jang, M.-K. Cho, H. Jang, J. Kim, J. Park, G. Kim, B. Kang, H. Jung, V. Umansky, and D. Kim, Single-Shot Readout of a Driven Hybrid Qubit in a GaAs Double Quantum Dot, *Nano Lett.* **21**, 4999 (2021).
- [15] L. Chen, H.-X. Li, Y. Lu, C. W. Warren, C. J. Krizan, S. Kosen, M. Rommel, S. Ahmed, A. Osman, J. Biznárová, A. Fadavi Roudsari, B. Lienhard, M. Caputo, K. Grigoras, L. Grönberg, J. Govenius, A. F. Kockum, P. Delsing, J. Bylander, and G. Tancredi, Transmon qubit readout fidelity at the threshold for quantum error correction without a quantum-limited amplifier, *npj Quantum Information* **9**, 1 (2023).
- [16] E. Champion, Z. Wang, R. Parker, and M. Blok, Multi-frequency control and measurement of a spin-7/2 system encoded in a transmon qudit (2024), arXiv:2405.15857 [quant-ph].
- [17] Z. Wang, R. W. Parker, E. Champion, and M. S. Blok, Systematic study of high $e\text{-}j/e\text{-}c$ transmon qudits up to $d = 12$, arXiv preprint arXiv:2407.17407 (2024).
- [18] R. Raussendorf and J. Harrington, Fault-tolerant quantum computation with high threshold in two dimensions, *Phys. Rev. Lett.* **98**, 190504 (2007).
- [19] J. Gambetta, W. A. Braff, A. Wallraff, S. M. Girvin, and R. J. Schoelkopf, Protocols for optimal readout of qubits using a continuous quantum nondemolition measurement, *Phys. Rev. A* **76**, 012325 (2007).
- [20] A. M. Gunyhó, S. Kundu, J. Ma, W. Liu, S. Niemelä, G. Catto, V. Vadimov, V. Vesterinen, P. Singh, Q. Chen, and M. Möttönen, Single-shot readout of a superconducting qubit using a thermal detector, *Nature Electronics* **7**, 288 (2024).
- [21] F. Vigneau, F. Fedele, A. Chatterjee, D. Reilly, F. Kuemmeth, M. F. Gonzalez-Zalba, E. Laird, and N. Ares, Probing quantum devices with radio-frequency reflectometry, *Appl. Phys. Rev.* **10**, 021305 (2023).
- [22] G. A. Oakes, V. N. Ciriano-Tejel, D. F. Wise, M. A. Fogarty, T. Lundberg, C. Lainé, S. Schaal, F. Martins, D. J. Ibberson, L. Hutin, B. Bertrand, N. Stelmashenko, J. W. A. Robinson, L. Ibberson, A. Hashim, I. Siddiqi, A. Lee, M. Vinet, C. G. Smith, J. J. L. Morton, and M. F. Gonzalez-Zalba, Fast high-fidelity single-shot readout of spins in silicon using a single-electron box, *Phys. Rev. X* **13**, 011023 (2023).
- [23] J. Stehlik, Y.-Y. Liu, C. M. Quintana, C. Eichler, T. R. Hartke, and J. R. Petta, Fast charge sensing of a cavity-coupled double quantum dot using a josephson parametric amplifier, *Phys. Rev. Applied* **4**, 014018 (2015).
- [24] F.-E. von Horstig, D. J. Ibberson, G. A. Oakes, L. Cochrane, D. F. Wise, N. Stelmashenko, S. Barraud, J. A. Robinson, F. Martins, and M. F. Gonzalez-Zalba, Multimodule microwave assembly for fast readout and charge-noise characterization of silicon quantum dots, *Physical Review Applied* **21**, 10.1103/physrevapplied.21.044016 (2024).
- [25] G. Burkard, T. D. Ladd, A. Pan, J. M. Nichol, and J. R. Petta, Semiconductor spin qubits, *Rev. Mod. Phys.* **95**, 025003 (2023).
- [26] D. J. Ibberson, L. Bourdet, J. C. Abadillo-Uriel, I. Ahmed, S. Barraud, M. J. Calderón, Y.-M. Niquet, and M. F. Gonzalez-Zalba, Electric-field tuning of the valley splitting in silicon corner dots, *Appl. Phys. Lett.* **113**, 053104 (2018).
- [27] G. Zheng, N. Samkharadze, M. L. Noordam, N. Kalhor, D. Brousse, A. Sammak, G. Scappucci, and L. M. K. Vandersypen, Rapid gate-based spin read-out in silicon using an on-chip resonator, *Nat. Nanotechnol.* **14**, 742 (2019).
- [28] N. W. Hendrickx, W. I. L. Lawrie, M. Russ, F. van Riggelen, S. L. de Snoo, R. N. Schouten, A. Sammak, G. Scappucci, and M. Veldhorst, A four-qubit germanium quantum processor, *Nature* **591**, 580 (2021).
- [29] N. Piot, B. Brun, V. Schmitt, S. Zihlmann, V. P. Michal, A. Apra, J. C. Abadillo-Uriel, X. Jehl, B. Bertrand, H. Niebojewski, L. Hutin, M. Vinet, M. Urdampilleta, T. Meunier, Y.-M. Niquet, R. Maurand, and S. D. Franceschi, A single hole spin with enhanced coherence in natural silicon, *Nat. Nanotechnol.* **17**, 1072 (2022).
- [30] A. Crippa, R. Ezzouch, A. Aprá, A. Amisse, R. Laviéville, L. Hutin, B. Bertrand, M. Vinet, M. Urdampilleta, T. Meunier, M. Sanquer, X. Jehl, R. Maurand, and S. De Franceschi, Gate-reflectometry dispersive readout and coherent control of a spin qubit in silicon, *Nature Communications* **10**, 2776 (2019).